Journal of Vibration Engineering & Technologies (2024) 12:2175–2203
https://doi.org/10.1007/s42417-023-00973-x

ORIGINAL PAPER

Experimental and Numerical Investigation on Soft Soil Tunnels Under Impact Loading Condition

K. Senthil[1] · **L. Pelecanos**[2] · **S. Rupali**[1] · **R. Sharma**[1] · **K. Manish**[1]

Received: 4 November 2022 / Revised: 26 March 2023 / Accepted: 7 April 2023 / Published online: 27 April 2023

Abstract

Background Tunnels extend the use of underground space for special applications such as transportation, mine development and civil defense. These structures could become susceptible to severe dynamic loads such as traffic loads, pile driving, impact and blast loads.

Methodology In this context, the experiment and simulations were conducted on semi-cylindrical tunnels of dimensions 1.2 m length × ∅ 0.5 m center-to-center and 0.05 m lining thickness under impact loading. The drop height was kept at 3.0 m and the burial depths of the soil cushion were varied as 0, 0.05, 0.10 and 0.15 m to study the effect of the cushion layer under repeated impact load. The experimental results were obtained in terms of damage to the tunnel and displacements in the tunnel under repeated impacts.

Results It was observed that the impact resistance of tunnels increased significantly when the natural burial depth increased from 0.05 to 0.10 m. It was concluded that the tunnel with 0.15 m burial depth was able to resist up to nine impacts as compared to the tunnel without cushion which offered resistance against two impact only. The numerical investigations were performed for each tunnel under repeated impacts using ABAQUS/Explicit. The numerical results were found to be in good agreement with the experimental results in terms of strain in rebar and mid displacement. The parametric study was performed for the influence of mass and velocity of the impactor in terms of crack pattern, impact force, displacement and energy absorption capacity in the tunnel. On increasing the mass of the impactor from 150 (4.41 kJ) to 400 kg (11.77 kJ), the energy absorption capacity was found to increase from 7.8% to 48.7%; however, on increasing the height of drop from 5 (5.1 kJ) to 20 m (20.40 kJ), the energy absorption capacity of the tunnel was increased from 8.1 to 48.6%.

Conclusions It was concluded that under the low-velocity impact, energy absorption in the tunnel is more sensitive to the mass of the impactor as compared to drop height. It was observed that Yang Qixin's algorithm was the best predicting algorithm among others when comparing peak impact force with the numerical result.

Keywords Reinforced concrete tunnels · Soil cushion · Impact load · Experiment · FE simulations

Introduction

The urban population is increasing at a steady pace and often leads to restricted and congested spaces. The resolution of constant conflict between the demand for infrastructures and the supply of residential spaces has often led to the idea of considering an ostensibly hidden means i.e., the underground space [1]. A tunnel is a superficial underground space that offers special applications such as transportation, mine development and civil defense. The construction and operation of the tunnel impose certain risks on all indirectly and directly involved parties in the project [2]. The underground structures are less vulnerable to seismic activities [3]. However, these structures become susceptible to severe dynamic loads such as traffic loads, pile driving, impact and blast loads. Regardless of the variations experienced by the structure under these dynamic loads, the elastic waves are the main transmitter of energies that cause vibrations in the system. Thus, it can be inferred that ground vibration mitigations are similar for each vibration source.

✉ K. Senthil
kasilingams@nitj.ac.in; urssenthil85@yahoo.co.in; urssenthil85@gmail.com

[1] Department of Civil Engineering, National Institute of Technology Jalandhar, Jalandhar, Punjab 144011, India

[2] Department of Architecture and Civil Engineering, University of Bath, Bath, UK

Tunnels are characterized as shallow tunnels which are on ground level and deep tunnels which are buried deep in the ground. Under static conditions, the shallow tunnels are subjected to overburden pressure from soil, in situ stresses and seepage of water. Soil pressure acts as an external factor that controls the final failure and deformation behaviour of concrete tunnels [4]. The dominant failure modes of reinforcing tunnels under static loading are structural failure due to plastic rotation of softening hinges, tensile failure caused by localized cracking and material failure due to concrete deterioration [5]. The tensile and compressive failure can occur in tunnel crown segments, and it was observed that maximum crown settlement can reach a rate of increase about 28%. It was suggested to provide local thickening of the support structure near tunnel interactions in order to improve the stability of tunnels [6, 7]. The circular shape of the tunnels is preferred in case of weak/soft ground due to their own ability to readjust during the subsequent load changes [8]. The underground structures not only endure static loads but also dynamic loads due to manmade or natural disasters. The impact or blast loading causes damage to the underground tunnel running beneath and affects the transportation system and human lives [9].

Under dynamic conditions, the tunnel is influenced by the seismic, impact, or blast loading. The underground tunnels suffer less damage than surface structures under dynamic conditions. It was reported that the damage in the tunnel decreases with increasing over- burden depth. Deep tunnels seem to be safer and less vulnerable to earthquake shaking than shallow tunnels [10]. Another factor is that tunnels constructed in soil are expected to suffer more damage compared to openings constructed in competent rocks. Under dynamic conditions, several types of damage were observed, including lining cracks, portal failures, spalling of the concrete lining, groundwater inrush, exposed and buckled reinforcement, displaced lining, rockfalls in unlined sections, lining collapses caused by slope failures, pavement cracks and lining shear-off [11].

Rockfall is the primary cause of impact loading on reinforced concrete (RC) tunnels. These impacts have been extensively studied using large-scale field test [12] as well as laboratory tests [13, 14]. The different mechanisms such as shear as well as the flexural failure of the structural elements were observed under impact load and provided a valuable database for the numerical analysis. It was observed that the deformation of the structure, the weight of the rock and the height of the rockfall were found to have a clear linear relationship. The inclination of slopes at the tunneling threshold often leads to the destabilization of rock faults which can induce serious damage to the tunnel structure.

The impact on reinforced concrete structures is often characterized as compression waves at the front side and strong tensile waves at the distal side. The impact on reinforced concrete tunnels is often studied on prototype models. Dhamne et al. [15] carried out physical modelling of D-shaped shallow tunnels to understand tunnel behaviour subjected to a high rate of impact loading (projectile). The deformations obtained in the prototype at the tunnel's crown are 100 times greater than those obtained in the scaled model. The impact energy, which is 105 times larger than the scaled model, is the reason for the increased magnitude of displacement. Gahoi et al. [16] investigated the deformation behaviuor of tunnels in rock subjected to impact loading. Important factors governing fracture and deformations in structural integrity were studied under the effect of cover depth and impact energy on shallow tunnel settlement. The reaction of the rock tunnel portal under impact loading, according to Zaid et al. [17] investigated the reaction of the rock tunnel portal under impact loading by varying overburden depth, impact energy and rock weathering grade. It was observed that the deformation behaviourr was found to be the same for overburden depth and rock weathering grade. Rao et al. [18] studied the effect of impact loading developed on shallow tunnels, due to projectile penetration. The probability of projectile penetration within the tunnel lining was observed to decrease as the tunnel's burial depth increased. Meng et al. [19] investigated the composite effect of steel fibre and rebar on full-scale steel fibre-reinforced concrete (SFRC) precast tunnel segments. The combined effect of steel fibre and steel rebar found increased load-carrying capacity by increasing the limit of proportionality and delaying the initial crack. Yan et al. [20] studied transient analysis of train-to-tunnel impact force using several parameters. The parametric investigation demonstrates that when the impact velocity rises, the dynamic response increases. Major tensile damage was also found in the impact zone, whereas compression damage was observed on the front, distal face of the damaged region. Sharma et al. [21] found that the tunnels having the lowest cover depth experience excessive deformation subjected to impact loading. Wang et al. [22] performed an experiment on intact and hollow sandstone against various confined pressure under dynamic compressive tests. In comparison to intact sandstone, the hollow cylindrical sandstone experienced lower dynamic strength and a significant critical strain. Wang et al. [23] developed a peridynamic model for reinforced concrete shed structures under rockfall impact. It was suggested that simplifying the impact force as the static load is not sufficient to understand the resistance of rock sheds under rock fall.

Various mitigation strategies were proposed to evaluate the structural resistance of tunnels. The active and passive open trench was used to control the vibrations [24]. It was also concluded that a larger trench was required at greater distances from the source to accomplish a given amplitude reduction. Bhatti et al. [25] constructed a three-layer Absorbent System (TLAS) and established a logical impact-resistant modelling methodology for arch-type shelters using the 3-D elastoplastic Finite Element Model (FEM) to compute the maximum input energy for obtaining the end state. When

TLAS was used as an absorption system, the transmitted impact force was reduced by half and the displacement at the pithead section was reduced by 75% at the crown, indicating that the RC arch tunnel's impact-resistant ability could be improved. Volkwein et al. [26] studied the use of a cushion layer to protect tunnels from impact loading since it is capable of dispersing impact energy and contact pressure to a large extent. Rezagholilou and Nikraz [27] observed that when the cushion layer thickness increases, the amount of the impact load reduces. Baziar et al. [28] conducted centrifuge experiments to investigate the impact-generated blast loading protection provided by geofoam barriers placed between the impact source and underground structures. The efficiency of such barriers against impact loading was found to be significant. Zaid et al. [29] used the finite element method to study the effects of impact loads on rock tunnels constructed in different regions in terms of unconfined compressive strength (UCS). The UCS of rock mass plays an important role in the stability of rock tunnels subjected to impact loading from falling rocks or other objects. The absolute value of the touch pressure was significantly reduced when the overlaying sand layer was used, according to Xu et al. [30] showing that the sand surface plays a significant role in minimizing the impact force. Layers of gravel can be used as a cushion for structures subjected to rockfalls. Based on probabilistic engineering, the gravel layer shall be used as an energy-absorbent element for rockfall protection [31].

Based on the detailed literature review, it was observed that rock fall is the major cause of dynamic damage to the tunnel structures, which needs in-depth evaluation. It was assessed that several mitigation strategies have been proposed in the earlier studies to resist the damage inflicted on the structures under dynamic loads. Nevertheless, the transient dynamic response of loose soil as a cushion layer for tunnel structures is an area of interest. Therefore, the current investigation was focussed on the reinforced concrete tunnels under low-velocity impact with and without the use of loose soil as a cushion. The numerical methods are then applied to validate and further study the effect of mass and impact energy on the resistance capability of the tunnel. "Experimental Investigation and Analytical Calculation Methods" highlights the experimental investigation along with sample preparation and free-falling drop weight test setup. "Constitutive Material Behavior and Numerical Modelling" discussed the constitutive and numerical modelling for different constituting materials using ABAQUS/CAE. "Comparison of Experimental and Numerical Results" highlights the validation and comparison of experimental and numerical investigations under repeated impact load. "Energy Absorption and Deformation on Tunnel using FE Simulations" highlights the energy absorption capacity and deformation of soil under various burial depths of the tunnel. The parametric investigations involving the mass and impact energy of the impactor are highlighted in "Influence of Mass and Velocity of Impactor".

Experimental Investigation and Analytical Calculation Methods

The experimental tests were conducted under low-velocity drop impact of hemispherical shape for burial depths varying from 0 to 0.15 m. The details of the test instrument and test procedure are explained in this section.

Experimental Program

The experiments were conducted on a semi-cylindrical tunnel with 1.2 m length × ∅ 0.5 m center-to-center and 0.05 m lining thickness to investigate the behaviourr of the tunnel to low-velocity impact under laboratory-led conditions. A semi-circular shape is the most commonly used modern underground structure [32], due to the conservative shape and lesser deformations in the RC tunnel. Also, the law of similitude has been applied to the impact force generated in the model in order to achieve the comparable force in the model to the actual field condition. The scaling up through the law of similitude for the mass of soil cushion which acts over the tunnel was not considered in the present study due to the insignificant mass of soil. The scale factor for different physical–mechanical parameters such as length, velocity, time, energy, acceleration, mass, strain, stress, elastic modulus and force available in the open source is shown in Table 1, which was drawn by [29]. Since the exact similarity of dynamic force is not feasible in the model, the most effective method for matching the model to the prototype is to feature certain similarities and subside others [33]. The similarity criterion used in this study follows the dynamic scale factor in linear elasticity such that, $C_E = C_\varepsilon = C_\sigma = 1$, where C_E is the scale factor of elastic modulus, C_ε is the scale factor of strain and C_σ is the scale factor of stress [34]. Using the above criteria, the energy was related to δ^4 for scaling the model to prototype as per [35]. All the tests were performed under the normal ambient condition with 1 g without applying any scaling to the soil cushion layer and/or without considering the scaling of geostatic stresses of the

Table 1 The law of similitude [34]

Parameter	Scale factor	Parameter	Scale factor
Length	δ	Mass	δ^3
Velocity	$\sqrt{\delta}$	Stress	1
Time	δ	Strain	1
Energy	δ^4	Elastic modulus	1
Acceleration	δ	Force	δ^2

soil. In general, the kinetic energies generated in the typical rockfall range up to 5000 kJ with a peak run-on distance of 18 m [36]. Also, the rockfall block velocities range from 30 to 40 m/s with a block mass of about 10 to 20 tons [37]. To develop 5000 kJ impact energy, the mass 104 kg impacted at a velocity of 9.81 m/s along with the scale factor $\delta = 6$ is relevant to cover 90% of rockfall impact events in practical projects. In the present study, the velocity considered in the model covers the practical rockfall event which is equivalent to 4000 kJ ($(mv^2/2)\ \delta^4 = 104 \times 7.67^2 \times 0.5 \times 6^4$) with an impact velocity of 7.67 m/s due to 3 m free-fall drop height ($\sqrt{2gh} = \sqrt{2 \times 9.81 \times 3} = 7.67$ m/s). Therefore, the scale factor $\delta = 6$ was selected as the controlled variable for the experimental program.

Specimen Preparation

The RC tunnel was constructed using M25 ($f_{ck} = 25$ MPa) concrete grade and ∅ 6 mm for longitudinal as well as lateral reinforcement. The concrete mix design was as per the recommendations of IS: 10262(2019) [38]. The tunnel was designed as per IS: 456(2000) [39] and the rebars were placed at 60 mm center-to-center for a reinforcement percentage of 0.4% as shown in Fig. 1a. The strain gauge, as illustrated in Fig. 1b was used to determine the strain in rebar for case T-1-BD0. Typical 120-Ω resistance strain gauge with a 10-mm gauge length and located at 0.6 m from the tunnel face, see Fig. 1c. Strain gauges were glued using cyanoacrylate (CN-Y) adhesives (post-yield). The data were recorded using a high-speed data acquisition system at a rated frequency of 50 kHz.

Test Setup

A typical image of the tunnel with and without a loose soil cushion layer was shown in Fig. 2a and b. The test setup consists of the free-falling impact test machine with a steel wire and a pulley mechanism was developed in the Department of Civil Engineering, NIT Jalandhar, see Fig. 2. The drop weight mechanism was supported by an inverted U-frame steel structure that had three numbers of concrete foundation pedestal of RC buried 1.2 m below the ground level and raised approximately 1 m above it. The drop height of weight was kept at 3 m for all the cases. The equipment was attached to the concrete using 0.01 m-thick base plates (0.203 × 0.203 m) and eight foundation bolts with a diameter of 0.012 m that were inserted 0.35 m deep. Using welded connections, four linked steel pipe channels of 3.4 m height and a diameter of 0.06 m were built on the base plates. Further reinforcement in the form of eight connections spaced by 0.06 m was given between the erected circular rods. To bear the moment created in the construction, steel cross sections were added to the steel beam in the form of lacing and battens, resulting in a monolithic structure. The structure holds two pulleys and a winch that allow the impactor to be raised to a height of 3 m from ground level using a mechanical hoisting mechanism and then free fall to impart impact loading to the specimen.

The impactor was made up of three plates measuring 0.25 × 0.2 × 0.025 m that encase a spherical solid steel ball with a diameter of 0.230 m and a hemispherical impactor head assembly, see Fig. 2c. The hemisphere nose shape impactor had a diameter of ∅ 8 mm, and the height of the cylindrical portion was 0.075 m. The weight of the impactor was 104 kg which was dropped from an effective height of 3 m. Through vast past experimental testing, the efficiency of the system was assumed to be approximately 98%, due to friction in the pulley. The tunnel rested on the soil bed with a specific weight of 1850 kg/m^3 and had no directional or rotational constraints. The experimental campaign for the testing of various tunnels under repeated impact loading is shown in Table 2. The designation "T" refers to the tested specimen number and "BD" refers to the Burial Depth of cushioned soil layer used in the experimental testing of tunnels in meters.

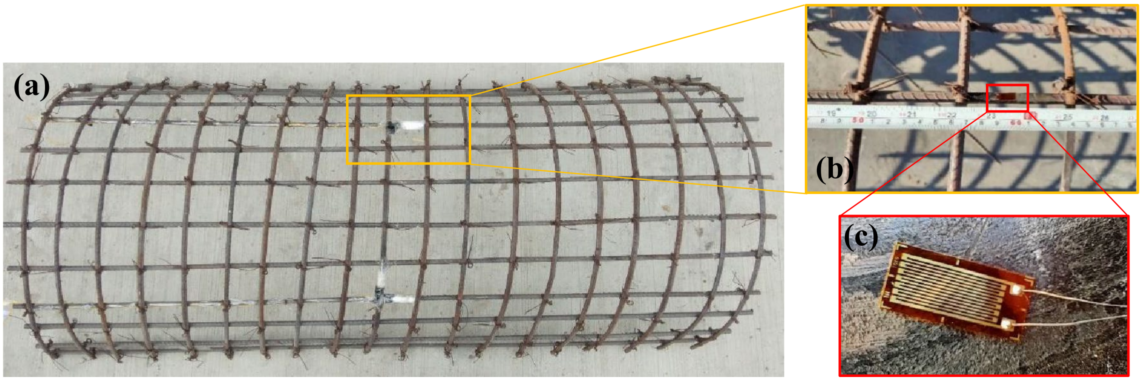

Fig. 1 Typical illustrations of **a** RC tunnel **b** location of strain gauge and **c** strain gauge

Fig. 2 Experimental setup of **a** bare tunnel **b** tunnel with soil cushion layer and **c** drop weight impactor

Table 2 Details of experimental program

Nomenclature	Burial depth, m	Impact velocity, m/s	Impact momentum, kg.m/s	Impact energy, J
T-1-BD0	0	7.67	797.68	3060.72
T-2-BD5	0.05	7.67	797.68	3060.72
T-3-BD10	0.10	7.67	797.68	3060.72
T-4-BD15	0.15	7.67	797.68	3060.72

The crack initiated as the impactor hits the tunnel and the compressive wave propagated at the front face of the tunnel. The cracks are then propagated due to reflective tensile stress waves. As per GB/T 16752–2017 [40], the allowable crack width under static conditions for sewer pipes was 0.2 mm and a length of 300 mm [41]. However, under impact scenarios, the crack widths are generally higher and depend on the strength of the concrete and concrete lining thickness. The limit for crack width for impact scenarios may be taken as (size of aggregate/2.5 = 12.5/2.5 = 5 mm) [42]. Further, in impact loading, the local damage predominates, and the cracks often originate from the location of impact and propagate towards the nearby supports. The width of a crack depends on the damage induced and the intensity of impact; however, the length of the crack is generally formed till the supports or longitudinal to the direction of bending. The direction of bending in a semi-circular-shaped tunnel under point-load impact takes place along the longitudinal direction towards the free end of the support. The failure is characterized as local shear failure due to complete loss of concrete material at the impact zone or the tensile crack width greater than 5 mm.

Analytical Methods for Rockfall Impact Force

The common calculation methods for peak rockfall impact force are the Swiss method [43], Japanese method [44], Australian method [31], B. S. Guan method [45] and the Method of Tunnel Manual [46]. The Swiss method is developed by Labiouse for rockfall impact force based on rockfall experiments.

$$F = 1.765.M_E^{2/5}R^{1/5}(QH)^{3/5}, \tag{1}$$

where M_E is the deformation modulus of the soil cushion layer, Q is the quality of the rockfall, and H is the falling height of the rockfall.

Japanese method is based on the Hertz elastic theory, the Japanese road association presented the relevant semiempirical and semi-theoretical calculation method of rockfall impact forces as follows:

$$F = 2.108.(Mg)^{2/3}\lambda^{2/5}(H)^{3}/5, \tag{2}$$

where g is the gravitational acceleration, λ is the lame constants, and ʋ is the Poisson's ratio of soil cushion layer.

Pichler et al. [31] has proposed a semiempirical and semi-theoretical method to measure the rockfall impact force, as follows, (Generally known as Australian method);

$$F = \frac{2Mv_0}{t_w};$$

$$\text{Impact time}, t_w = 2L/v_0, \tag{3}$$

where t_w is the impact time of the rockfall, D is the diameter of the rockfall, M is the mass of the rockfall and v_0 is the velocity of rockfall.

In 1996, B S Guan established the empirical method of impact force based on laboratory tests. This method considers the influence of the thickness of the soil cushion layer on the impact force.

$$F = \zeta Ma;$$

$$\text{Acceleration}, a = \frac{\sqrt{2gH}}{t_w}\text{and}$$

$$\text{Impact time}, t_w = \frac{1}{100}\left[0.097\text{Mg} + 2.21h + \frac{0.045}{H} + 1.2\right], \tag{4}$$

where ζ is the correction coefficient of the rockfall impact force, a is the acceleration of the rockfall impact, and h is the thickness of the soil cushion layer.

The method of tunnel manual refers to an approach recommended in Technical Manual for Railway Engineering Design Tunnel, and in essence, it is also an approximation method of the theorem of momentum.

$$F = \frac{Qv_0}{gt_w};$$

$$\text{Impact time}, t_w = \frac{2h}{c};$$

$$\text{Compression wave velocity}, c = \sqrt{\frac{(1-\nu)}{(1+\nu)(1-2\nu)}\cdot\frac{E}{\rho_0}}, \tag{5}$$

where c is the reciprocating velocity of compression waves in the soil cushion layer, E is the modulus of elasticity of the soil cushion layer, ν is Poisson's ratio and ρ_0 is the density before the deformation of the spherical cavity microbody.

Constitutive Material Behavior and Numerical Modelling

The material model for the concrete, steel rebar and soil were defined using concrete damage plasticity, Johnson–Cook and Drucker Prager model, respectively, using ABAQUS finite element software is discussed in this section. Detailed numerical modelling was also discussed in this section.

Concrete Damage Plasticity (CDP) Model for Concrete

The CDP model uses the concept of isotropic damaged elasticity combined with isotropic tensile and compressive plasticity to represent the inelastic behavior of concrete. This model allows the definition of strain hardening in compression and can be defined as sensitive to strain rate, thus resembling the impact phenomenon more realistically. The model was developed by Lubliner et al. [47] and, later modified by Lee and Fenves [48] for dynamic and cyclic loading and adopted in ABAQUS/EXPLICIT.

The CDP model can be defined in terms of stress–strain response as follows:

$$\sigma_t = \left(1 - d_t\right)D_0^{el} : \left(\varepsilon - \varepsilon_t^{el}\right) \tag{6}$$

$$\sigma_c = \left(1 - d_c\right)D_0^{el} : \left(\varepsilon - \varepsilon_c^{el}\right), \tag{7}$$

where t is tension, c is compression, σ is stress vectors, ε^{el} is plastic strains, d is the damage function of plastic strain and D_0^{el} is the initial undamaged elastic modulus.

The model is idealized as homogeneous and isotropic due to the simplicity of modelling technique and similar elastic moduli observed in compression and tension stress–strain diagrams. The CDP model considers non-associated plastic flow rules. The non-associative plastic flow rule has been characterized as

$$G_p = \sqrt{\left(\varepsilon\sigma_{t0}tan\psi\right)^2 + \left(\frac{3}{2}s : s\right)} - \overline{p}tan\psi, \tag{8}$$

where ψ represent the dilation angle and σ_{t0} as uniaxial tensile stress at failure and ε as eccentricity. The eccentricity parameter, m of the flow potential, ε with a value of 0.1 has been found by comparing the experimental data from bi- and triaxial strength results [48]. The compressive and tensile damage parameters, $D_c\left(\tilde{\varepsilon}_c^{pl}\right)$ and $D_t\left(\tilde{\varepsilon}_t^{pl}\right)$ can be characterized using the degraded elastic compressive and tensile stiffness as $\left(1 - D_c\right)E_c$ and $\left(1 - D_t\right)E_c$ respectively, where E_c is modulus of elasticity. The material damage is characterized from zero to one with zero being undamaged and one as completely damaged. The material model parameters used in this study are based on the studies of [49–51] and are shown in Tables 3 and 4.

Johnson–Cook Model for Reinforcement Bar

The Johnson–Cook model [52] was used to define the behavior of the ductile materials and is used in the present study to define the strength and fracture behavior possessed by the steel reinforcement bars. The Johnson–Cook model is based on the strain hardening principle and von-mises yield criteria. The equivalent von Mises yield stress is therefore expressed as follows:

$$\overline{\sigma} = \left[\mathrm{A} + \mathrm{B}\left(\overline{\varepsilon}^{\mathrm{pl}}\right)^{n}\right]\left[1 + \mathrm{C}\ln\left(\frac{\dot{\overline{\varepsilon}}^{\mathrm{pl}}}{\dot{\varepsilon}_0}\right)\right]\left[1 - \hat{\mathrm{T}}^{\mathrm{m}}\right], \tag{9}$$

where $\overline{\varepsilon}^{\mathrm{pl}}$ is equivalent plastic strain, A, B, n and m, are material parameters measured at or below the transition temperature, $\mathrm{T_o}$. There are various constants used to define the Johnson–Cook model for steel, which comprises yield strength, strain hardening coefficient, strain hardening exponent, strain rate sensitivity and thermal softening parameter. The Johnson–Cook material parameters based on the study by Iqbal et al. [53] and Kumar et al. [54] were considered for the present study and are tabulated in Table 5.

Drucker Prager Model for Soil

Drucker Prager model [55] was used to define the behavior of the soil part. The yield area in this model consists of two main areas, i.e., the fracture area providing the flow cut and the cover, crossing the equivalent pressure. This model simplified the Mohr–Coulomb model by substituting the hexagonal-shaped failure cone with a simple failure cone. The Drucker-Prager hardening behavior is defined by yield stress versus absolute plastic strain values. The Drucker-Prager can be illustrated as follows:

$$F = \frac{q}{2}\left[1 + \frac{1}{K} - \left(1 - \frac{1}{K}\right)\left(\frac{r}{q}\right)^{3}\right] - p^{'}\tan\beta - d = 0, \tag{10}$$

where q is the deviatoric stress tensor, $p^{'}$ is mean stress, K determines the yield surface shape and maintains its convexity in the deviatoric (π) plane, r is the third deviatoric stress

Table 3 Multi-axial behaviour of CDP model [49]

Parameter	Value
Density, ρ (kg/m^3)	2400
Young's modulus, E (N/m^2)	24×10^9
Poisson's ratio, μ	0.15
Dilation angle	30°
Eccentricity, m	0.1
K	0.66
f_{b0}/f_{c0}	1.16

Table 4 Uni-axial compressive and tensile behavior of CDP model [49]

Yield stress (N/m^2) × 10^6	Inelastic strain (m/m)	Damage parameter
Compressive behavior		
21	0	0
20	0.0011	0.20
19	0.0040	0.50
Tensile behavior		
3.3	0	0
3.2	0.003	0.50
3.1	0.005	0.55
3	0.007	0.61
2.9	0.010	0.67

Table 5 Johnson–cook model parameters for steel Fe 415 [53, 54]

Description	Parameters
Density, ρ (kg/m^3)	7850
Young's modulus, E (N/m^2)	200×10^9
Poisson's ratio, μ	0.33
Yield stress constant, A (N/m^2)	493×10^6
Strain hardening constant, B (N/m^2)	383×10^6
n	0.45
Viscous effect, C	0.0114
Thermal softening constant, m	0.94
Reference strain rate, $\dot{\varepsilon}$	0.0005
Melting temperature (K)	1800
Transition temperature (K)	293
Fracture strain constant	
D_1	0.0705
D_2	1.732
D_3	− 0.54
D_4	− 0.015
D_5	0

tensor invariant, β is related to internal friction (φ) angle for no dilatancy stage given by

$$\tan\beta = \frac{\sqrt{3}\sin\varphi}{\sqrt{1 + \left(\frac{1}{3}\right)\sin^2\varphi}} \tag{11}$$

And d is the hardening parameter related to cohesion (c) given by

$$\frac{d}{c} = \frac{\sqrt{3}\cos\varphi}{\sqrt{1 + \left(\frac{1}{3}\right)\sin^2\varphi}} \tag{12}$$

The dilation angle calculation is based on the studies of [56, 57] and it is preferable to keep it at 0 degrees. However, the value of the dilation angle is considered as 1° because the strength and dilatancy rate reduction that takes place in dense soils must be considered when dealing with problems involving geotechnical stability [58]. The corresponding Drucker Prager model parameters used in this study are given in Table 6.

Table 6 Material constant for soil [49, 56, 57]

Density (kg/m^3)	Elastic modulus (N/m^2)	Poisson ratio	Dilatation angle (°)	Angle of internal friction (°)	Flow stress ratio
1850	20.9×10^6	0.36	1	31	0.778

Finite Element Modelling

Numerical investigations and modelling of the assembly were carried out using ABAQUS/CAE. A typical assembly for 0.15 m burial depth is shown in Fig. 3. The model was based upon the Lagrangian formulation, and the tunnel and buried soil were modelled as three-dimensional deformable bodies as shown in Fig. 3b, c. The main and transverse reinforcement was provided with 6 mm-diameter bars, placed at a spacing of 0.06 m centre to centre, in proximity to the experimental condition. The impactor was modelled as an analytical rigid body with a mass inertia of 104 kg was assigned to it as shown in Fig. 3d. The shape of the impactor was semi-spherical and the contact between various bodies was given using general contact for all exterior surfaces. The tangential contact was given using the Coulomb friction model with a coefficient of friction of 0.30 and normal HARD contact was used. The embedded constraint

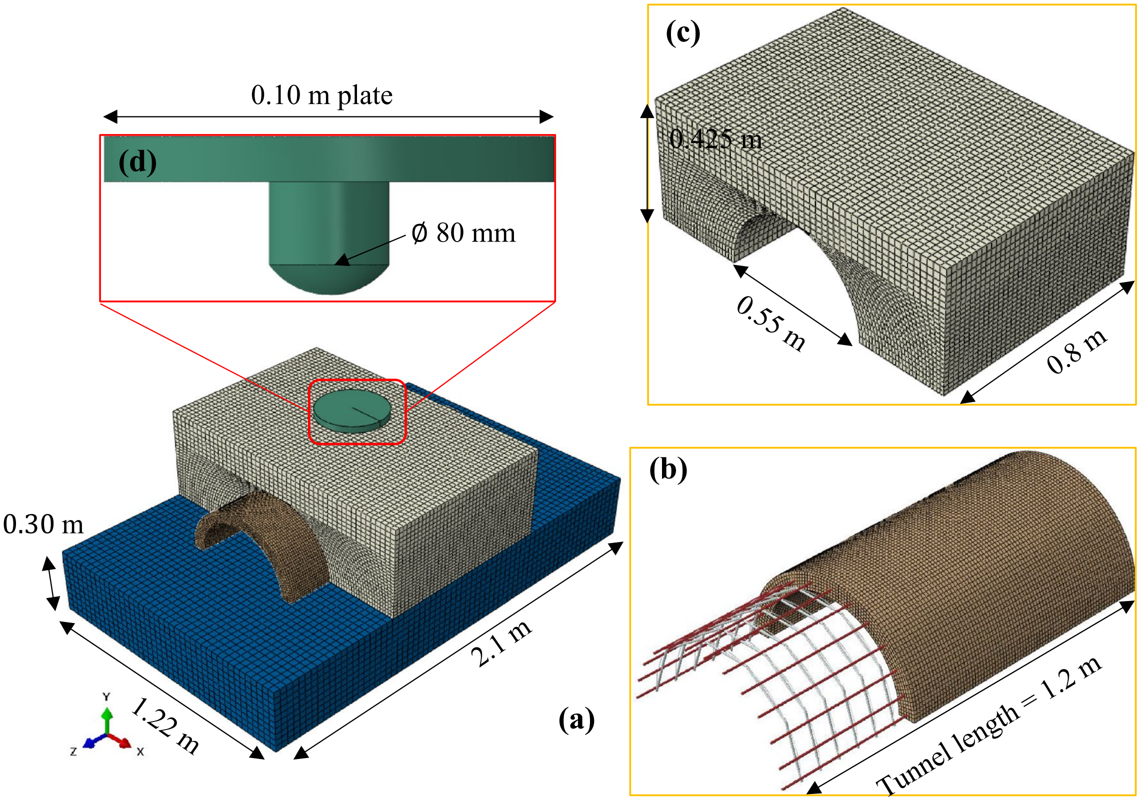

Fig. 3 **a** Assembly of the model **b** embedded rebar **c** burial soil and **d** rigid impactor

was used to model the interaction between the concrete and steel rebar. The bottom soil was fixed, and all degrees of freedom were restrained. The burial soil was restrained from motion in the x-direction. The tunnel was restricted in the z-direction and corresponding rotational degrees of freedom were also restricted. The impactor was given an initial velocity of 7.67 m/s. The mesh for 3-D deformable bodies was C3D8R, an 8-noded linear brick element with reduced integration. For reinforcement, a 2-node linear beam in space (B31) element was used. A mesh size of 20 mm was provided for both longitudinal and transverse reinforcement.

The sensitivity of the mesh size was studied on tunnel T-1-BD0 against a 3-m drop height. A detailed mesh convergence has been performed to study the effect of mesh size in the concrete corresponding to mesh sizes of 20, 15, 12, 10, 7.5 and 6 mm. The results in terms of the peak tunnel displacement in the downward direction at the point of impact were used for mesh convergence. The peak displacement on the tunnel with 20, 15, 12, 10, 7.5 and 6 mm mesh size was found to be 21, 28, 29, 34 and 33 mm, respectively. The optimum mesh is taken as 7.5 mm based on the mesh convergence study as the computational cost increased by 1.74 times for 6 mm mesh as compared to 7.5 mm mesh whereas the variation in displacement is 2.9%. Therefore, keeping the computational cost, a mesh size of 7.5 mm is chosen for the numerical simulations. Figure 4a. For numerical validation, the predicted micro strain on the tunnel longitudinal reinforcement bar with varying mesh size was compared with the experimental results, see Fig. 4b. The peak strain was found to be 66, 133, 207, 174 and 196 and 231 µℇ on the tunnel with 20, 15, 12, 10, 7.5 and 6 mm mesh size, respectively, whereas the measured peak strain was found to be 169.36 µℇ which is close to the simulation results of mesh size of 10 mm. However, the peak midpoint displacement was found closer to 7.5 mm, i.e., 34 mm rather than 10 mm mesh size i.e., 29 mm as compared to experimental results, i.e., 32 mm. The difference in results could be attributed to the absence of strain rate consideration in the model. Further, the compressive fracture energy of concrete is not taken into account concerning the change in mesh size.

Comparison of Experimental and Numerical Results

The damage pattern on all four tunnels observed from the experiment was compared with the numerical simulations. The resistance offered by the tunnels with different burial depth cases against impact loading of 3 m drop height was compared. The compression, as well as tension damage in the tunnel, was quantified and the damage mechanism involved in the dynamic event was discussed.

Comparison of tunnel T-1-BD0

The tunnel T-1-BD0 was studied under a 3 m drop height and the sample resisted up to two impacts until complete concrete failure at the impacted location. For the first impact,

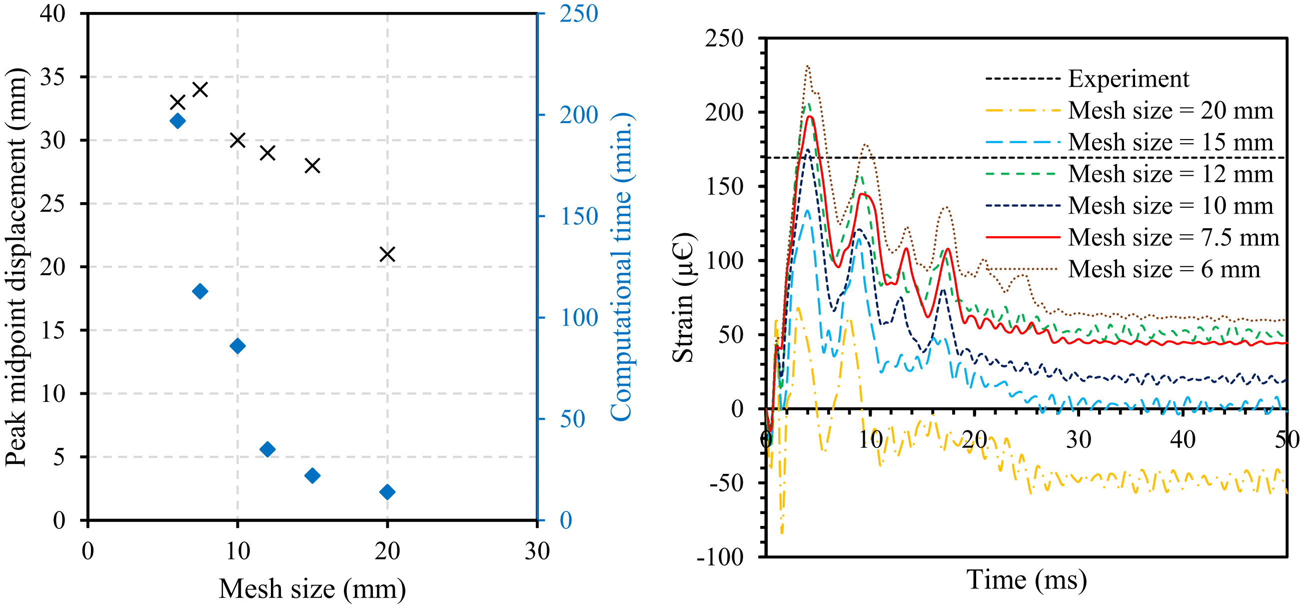

(a) **(b)**

Fig. 4 **a** Mesh convergence study on tunnel and **b** prediction of strain in reinforcement for T-1-BD0

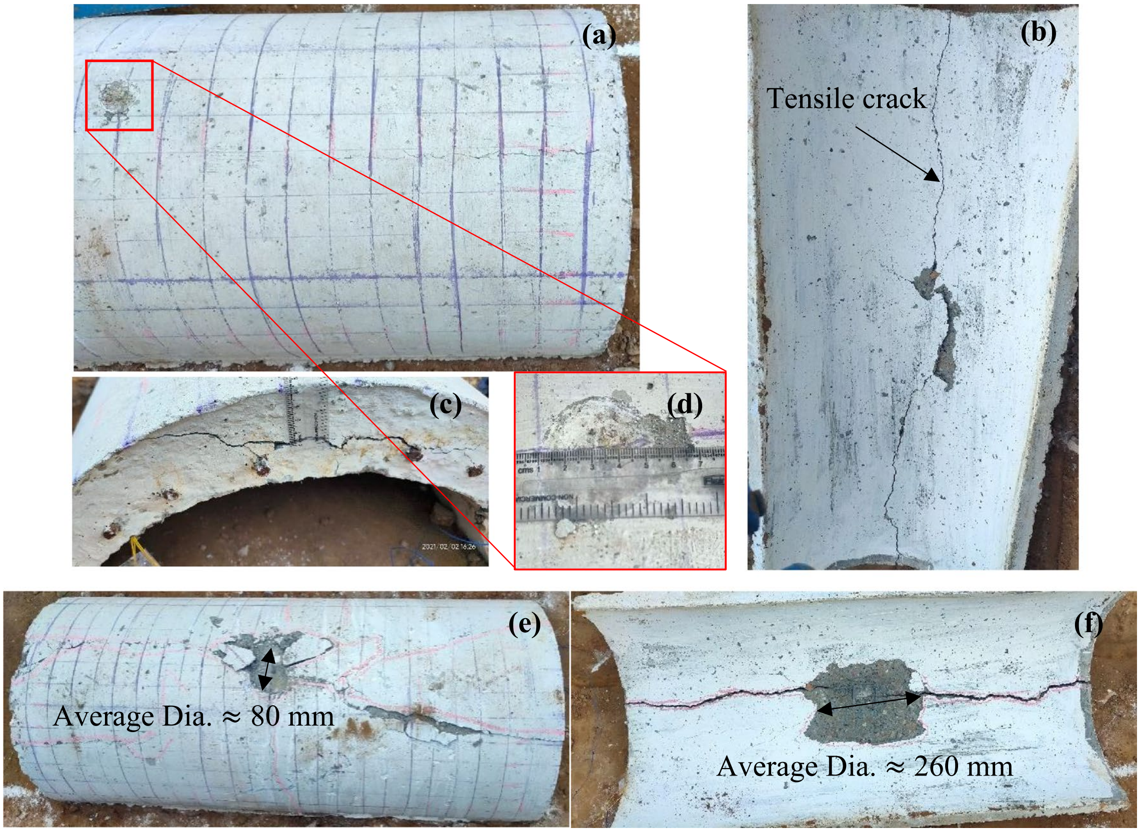

Fig. 5 Damage to specimen T-1-BD0 at 1st impact for **a** front, **b** rear, **c** side face, **d** front crater and for 2nd impact at **e** front face and **f** rear face

the tunnel experiences a frontal crater with a longitudinal crack, see Fig. 5a. The rear face experiences longitudinal flexural cracks with an average width of 2.5 mm, see Fig. 5b. Lateral cracks were experienced for the side face where the maximum crack width was 2 mm, see Fig. 5c. The average diameter of the crater was 40 mm, see Fig. 5d. The scabbing and spalling phenomenon was observed for both the rear and front faces respectively. The major failure of the tunnel was a flexural failure due to tensile waves at the rear face. The same can be observed for tensile and compression damage in the numerical study, see Fig. 6(a–i)-(b–ii). For the second impact, major damage occurred to both front as well as rear faces. For the front face, the crater diameter expanded to 80 mm and major longitudinal damage was observed, see Fig. 5e. For the rear face, the major failure was punching shear at the location of impact along with a flexural crack, see Fig. 5f. The scabbing observed at the rear face has an average diameter of 260 mm. The tunnel completely failed at the point of impact and one major crack propagated longitudinally along both faces and further enlarged the cracks at the side faces. The punching shear failure occurs at a shear angle of 32° indicating severe damage to the rear face of the tunnel. The same was observed for numerical simulation where severe compression damage to the front face along with longitudinal tensile damage at the rear face was observed, see Fig. 6a–ii, b–iv. The radial damage was equivalent for both the faces in numerical simulation, see Fig. 6a–v, b–v. The peak deformation in rebar was 30 mm and 51.2 mm corresponding to the first and second impacts. It was observed that the deformation in concrete was well above the complete damage state which was obvious from the deformation in rebar.

Comparison of Tunnel T-2-BD5

The tunnel T-2-BD5 was tested under similar loading conditions for a soil cushion layer thickness of 0.05 m. The tunnel was able to take three impacts before complete failure. During the first impact, the impactor completely perforated the soil cushion layer and impacted the tunnel. The damage to the tunnel was visible in the form of the side face radial cracks of width 1–2 mm, see Fig. 7a. The damage to the rear face of the tunnel experiences a longitudinal flexural crack that propagated along the whole length of the tunnel, see Fig. 7b. The width of the cracks was approximately 3 mm. The front face of the tunnel experiences compression damage with crater formation whose diameter is ∅ 30 mm. The numerical model was able to correctly capture

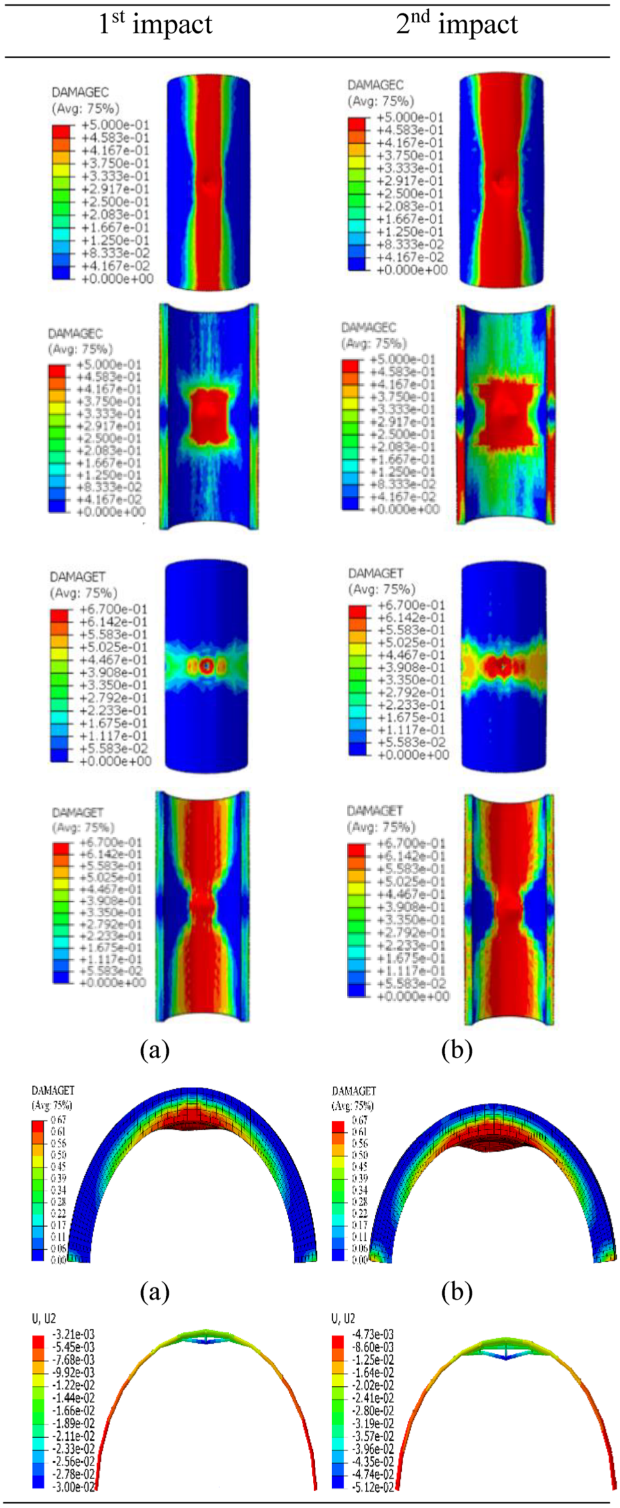

Fig. 6 Compression and tension damage to the tunnel T-1-BD0 at front and rear face under repeated impacts **a** side face and **b** displacement in rebar

the damage on the tunnel front and rear surface, see Fig. 8. It was observed that the compression damage in the tunnel occurred radially at the front face, whereas the tensile wave propagated longitudinally at the rear face of the tunnel, see Fig. 8. As the number of impacts increases, the width of crack increases; however, no change in the length of crack was observed.

Under the second impact, the radial cracks get enlarged, see Fig. 7c and scabbing was observed at the rear face of the tunnel. The longitudinal cracks got wider at the rear face, see Fig. 7d. The size of the frontal crater was approximately equal to the diameter of the impactor, i.e., 75 mm. A similar pattern was observed for numerical results where longitudinal compressive waves induce damage to the front face whereas punching shear failure was formed at the rear face of the tunnel. It was observed that compressive and tensile waves cause similitude of damage at the front and rear face respectively, see Fig. 8. From the numerical study, it was evident that the damage to the tunnel occurred as longitudinal flexural cracks as well as punching shear failure. The 0.05 m burial depth was proven to be ineffective for low-velocity impact loading based on the current investigations. In the case of the third impact, severe damage was observed on both sides of the tunnel. The front face has severe spalling and crater formation occurred whose diameter was 80 mm and further concrete was completely eroded from the impact zone, see Fig. 7e. The rear face of the tunnel experiences severe scabbing of concrete with many flexural crack formations, see Fig. 7f. The scabbing diameter was approximately equal to 300 mm. The punching shear failure occurs at a shear angle of 27° indicating severe damage to the rear face of the tunnel. The side face experiencing tensile damage in numerical simulations was like an experimental pattern as shown in Fig. 8. The downward displacement on the rebar for the first, second and third impact was 26, 39 and 56 mm, respectively. It was observed that the deformation in concrete was well above the complete damage state which was obvious from the deformation in rebar.

Comparison of Tunnel T-3-BD10

The tunnel T-3-BD10 was tested under similar loading conditions for a soil cushion layer thickness of 0.1 m. The tunnel sustained eight impacts before complete failure. From the first to fifth impact, minor side face cracks were formed in the tunnel and the width of the cracks formed was increased from 1 to 3 mm. It was observed that the 10-mm soil cushion layer had a significant effect on the impact resistance under impact loading. The soil layer was able to resist the impact and prevent damage to the tunnel till the fourth impact. There were no side face cracks observed in the T-2-BD10 tunnel till the fifth impact, see Fig. 9a–d. For the fifth impact, the radial cracks with a width of 3 mm were formed, see Fig. 9e. For the sixth impact, the target was completely perforated the cushion layer of soil at the impact zone and flexural cracks were developed on the rear face and

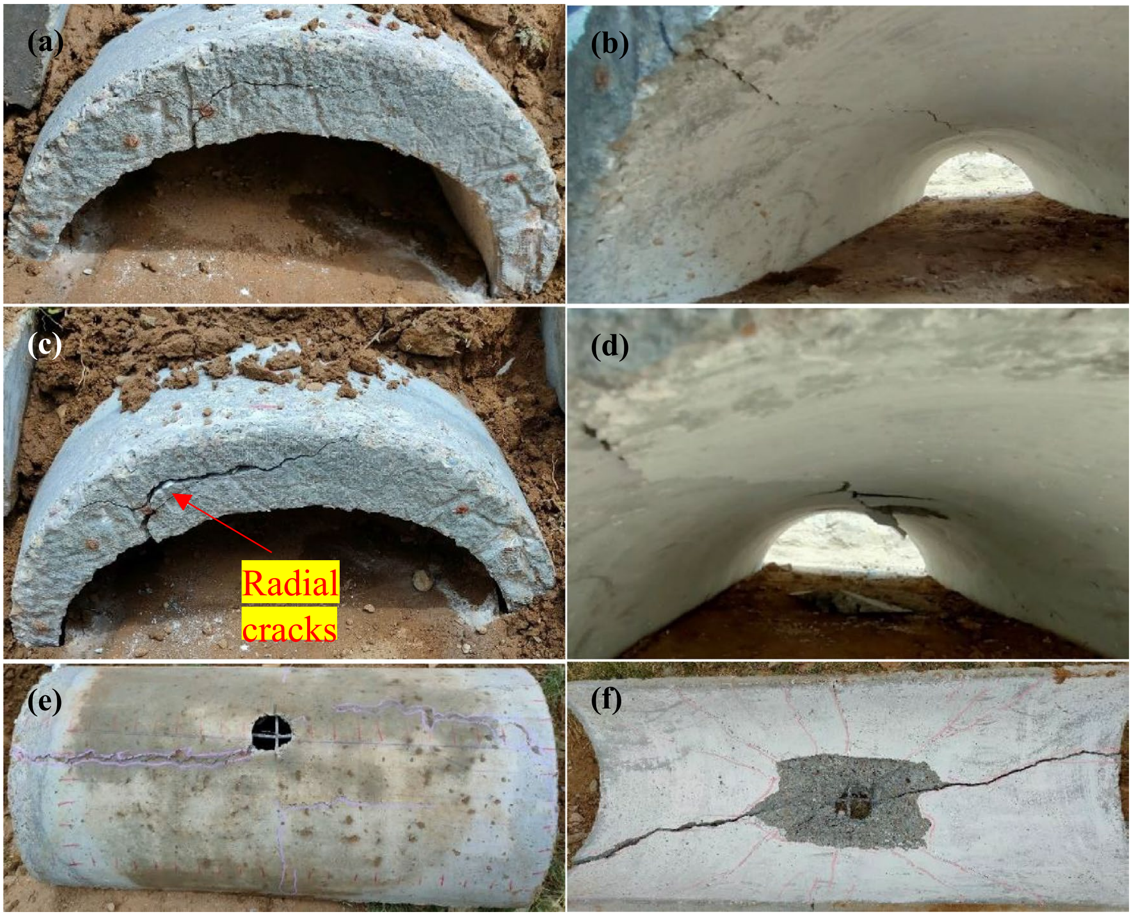

Fig. 7 Damage to the tunnel T-2-BD5 under (**a**), **b** 1st impact (**c**), **d** 2nd impact and (**e**), **f** 3rd impact

extended to the side face of the tunnel, see Fig. 9f–I, f–ii. A similar damage pattern with enlarged cracks was observed during the seventh impact, see Fig. 9h–I, h–ii. The soil was completely deformed and moved away from the impact zone during the fifth and sixth impacts, see Fig. 9g, j.

During eight impacts, severe damage was observed for the tunnel at the front as well as the rear face, see Fig. 9k, l. The impactor was able to fully penetrate the front face where crater formation was observed with a diameter equal to the impactor diameter. Also, the spalling of concrete was observed at the tunnel ends. At the rear face, damage to the tunnel had large scabbing with an average diameter of 280 mm. The punching shear failure occurs at a shear angle of 29° indicating severe damage to the rear face of the tunnel. The numerical simulation was performed till the fourth impact in comparison with the experimental results. The numerical simulation was able to correctly capture the experimental results. However, the damage to the tunnel was overpredicted and it had only four impacts for the tunnel to fail. The radial cracks were correctly captured in the numerical simulation, see Fig. 10. The deformation in the tunnel rebar for four impacts increased from 5.3 mm to 53 mm.

Comparison of Tunnel T-4-BD15

The tunnel T-3-BD15 was tested under similar loading conditions for a soil cushion layer thickness of 0.15 m. The tunnel sustained nine impacts before complete failure. From the first to sixth impact, minor cracks were formed in the tunnel side face and the width of cracks was found to increase from 1 to 3 mm. It was observed that the 0.15-m soil cushion layer had a significant effect on the impact resistance under impact loading. The soil layer was able to resist the impact and prevent damage to the tunnel till the fifth impact. There were no side face cracks observed in the T-2-BD15 tunnel till the fifth impact. For the fifth impact, the radial cracks with a width of 2 mm formed on the side face, see Fig. 11a–i. Similarly, rear face cracks were formed whose width is 5 mm, see Fig. 11a–ii. During the sixth impact, the side face cracks were found enlarged, see Fig. 11b–i, and further rear face scabbing of concrete was observed, see Fig. 11b–ii. After the sixth impact, the tunnel damage was quite severe where no cushion layer was available at the impact location to dissipate the energy. The cracks at the side face were found enlarged during the seventh and eighth

Fig. 8 Compression and tension damage to the tunnel T-2-BD5 at front and rear face under repeated impacts (**a**) side face and (**b**) displacement in rebar

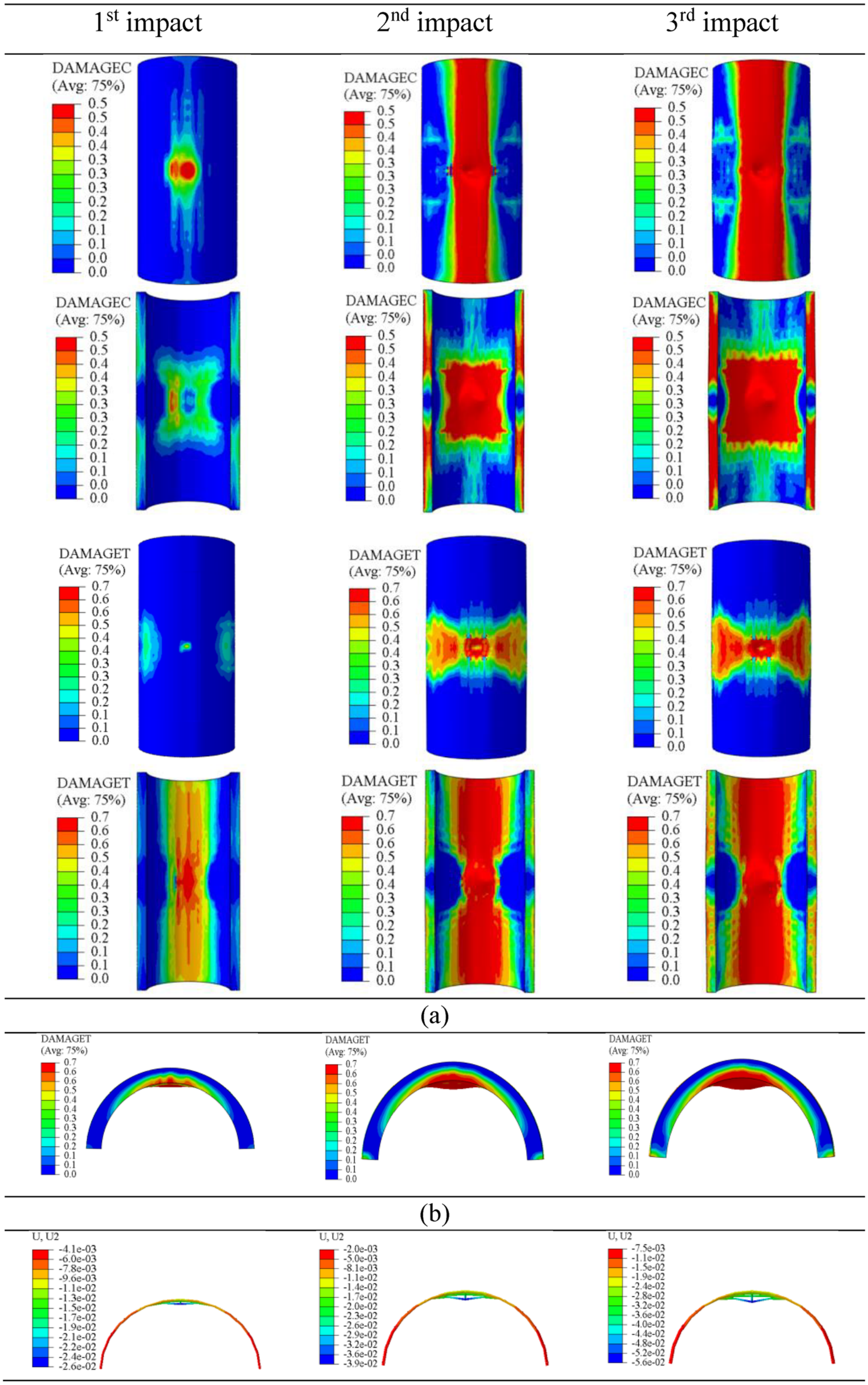

impact, see Fig. 11c–I and d–i and a large mass of concrete was found scabbed at the rear face, see Fig. 11c–ii and d–ii.

During the ninth impact, severe damage was observed to the tunnel at the front as well as the rear face, see Fig. 11e, f. The impactor was able to fully penetrate the front face where crater formation was observed with a diameter equal to the impactor diameter. However, no spalling of concrete was observed at the tunnel ends. The longitudinal compressive wave was the primary cause of flexural failure at the front surface of the tunnel. The crater diameter at the front

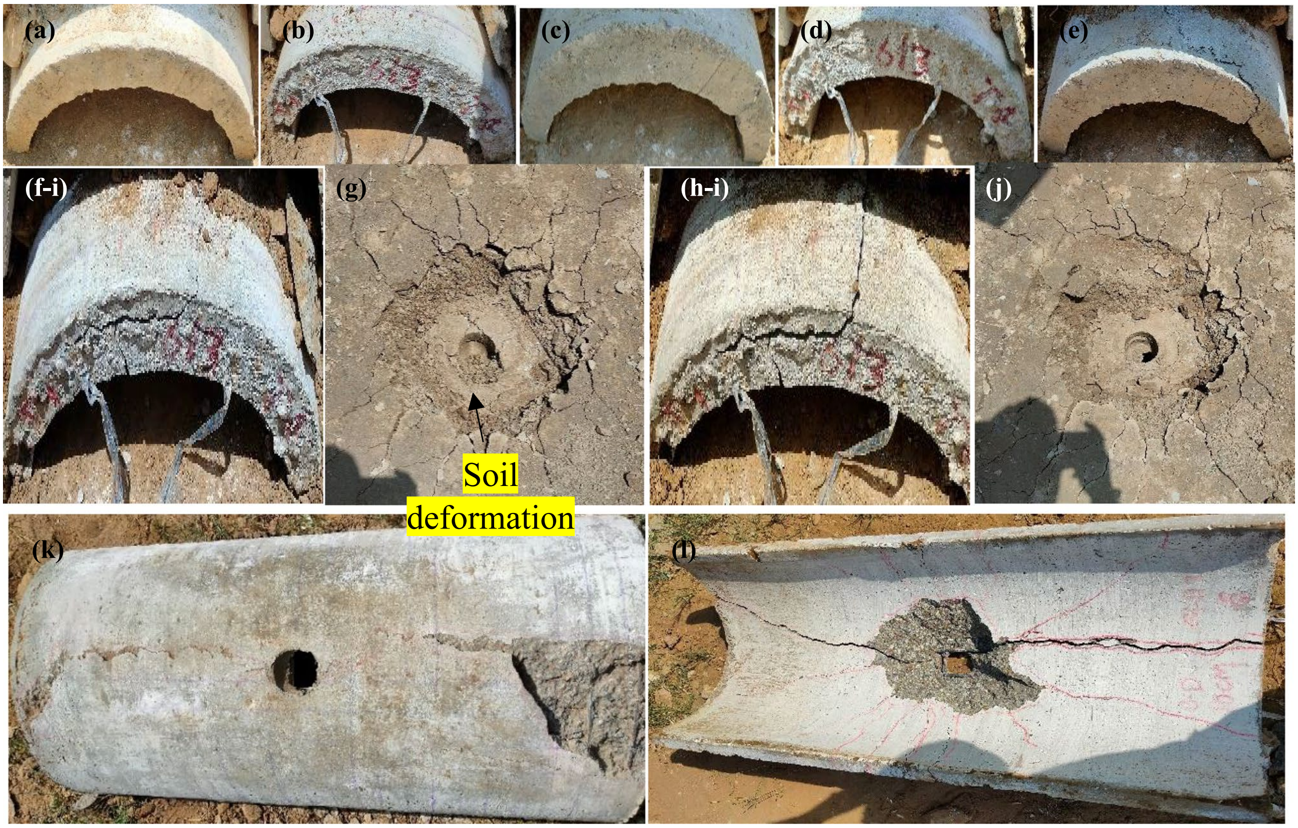

Fig. 9 Damage to tunnel side face (**a**–**e**) 1st impact to 5th impact, **f**–**i** 6th impact, **g** damage to soil cushion layer for 6th impact, **h**–**i** damage to side face for 7th impact **j** damage to damage to soil cushion layer for 7th impact and **k** & **l** front and rear face damage on 8th impact

face had a diameter of 75 mm. At the rear face, damage to the tunnel had large scabbing with an average diameter of 360 mm. The punching shear failure occurs at a shear angle of 21° indicating severe damage to the rear face of the tunnel. The numerical simulation was performed till the 4th impact in comparison with the experimental results. The numerical simulation was able to correctly capture the experimental results, see Fig. 12. The radial cracks were correctly captured in the numerical simulation, see Fig. 12. The deformation in the tunnel rebar was found to increase from 5.3 to 53 mm from first to fourth impacts.

Energy Absorption and Deformation on Tunnel using FE Simulations

The predicted energy absorption capacity was compared for each cushion layer thickness and further extended numerically to 0.30 m burial depths. The stress in tunnel and deformation that occur in rebar was also studied for varying burial depths and discussed in this Section. Further, the deformation in bed soil was also compared against each burial depth and discussed.

Energy Absorption Capacity Under Repeated Impact Load

The load versus displacement response of tunnels under varying burial depths for repeated impacts was presented in Fig. 13. The depth of the cushion layer was extended to 0.3 m for numerical study. The peak impact force for various burial depth cases under repeated impacts is presented in Table 7. The peak impact force for zero burial depth was found to be 95.55 kN and the corresponding peak mid-node deformation was 46.48 mm. The calculated impulse and energy absorption capacity of the zero burial depth tunnel was 0.85 kN-s and 2998.62 kN-mm, respectively, see Table 7. During the second impact, the peak impact force increased to 110.38 kN and the peak displacement was 79.34 mm, see Table 7. The corresponding impulse and energy absorption capacity was 0.91 kN-s and 2912.05 kN-mm, respectively. It was observed that the peak impact force, as well as impulse, was increasing with the second impact whereas energy absorption was similar. The rise in peak impact force with repeated impact was also found because of the contact between the impactor and concrete part and increased values of plastic strains than strain at failure resulting in over elongation of elements [59]. The force–displacement plot for the 0.05-m

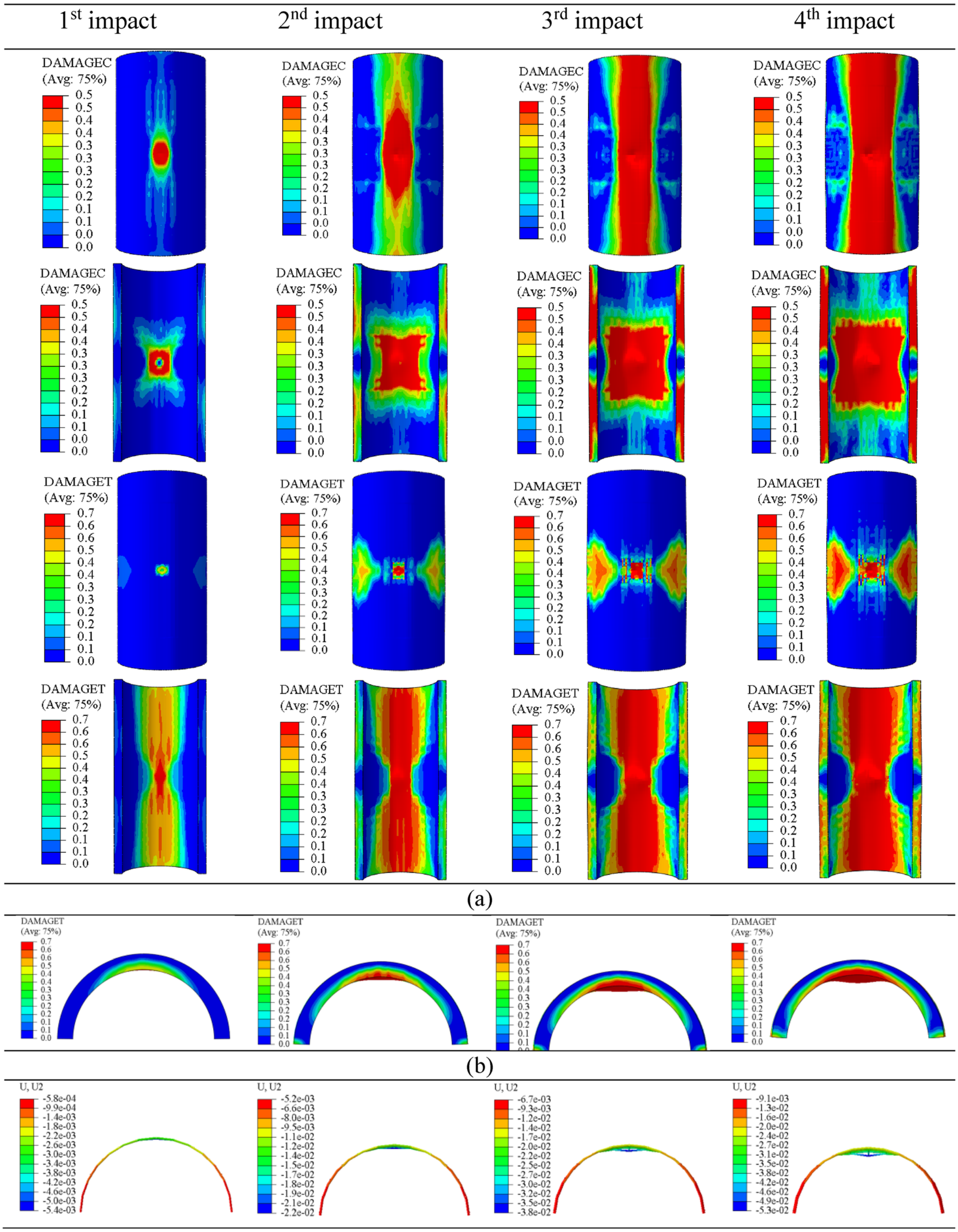

Fig. 10 Compression and tension damage to the tunnel T-3-BD10 at front and rear face under repeated impacts **a** rear face and **b** displacement in rebar

burial depth case is shown in Fig. 13a. For 0.05 m burial depth, the peak impact force and displacement for 1st impact were found to be 204.32 kN and 35.27 mm, respectively. For the 2nd and 3rd impact, the peak impact force was increased to 221.41 kN and then reduced to 200.65 kN. The peak displacement for the 2nd and 3rd impact was found to be 56.87 and 73.88 mm corresponding to the initial position. The impulse and energy absorption capacity of 0.05 m burial

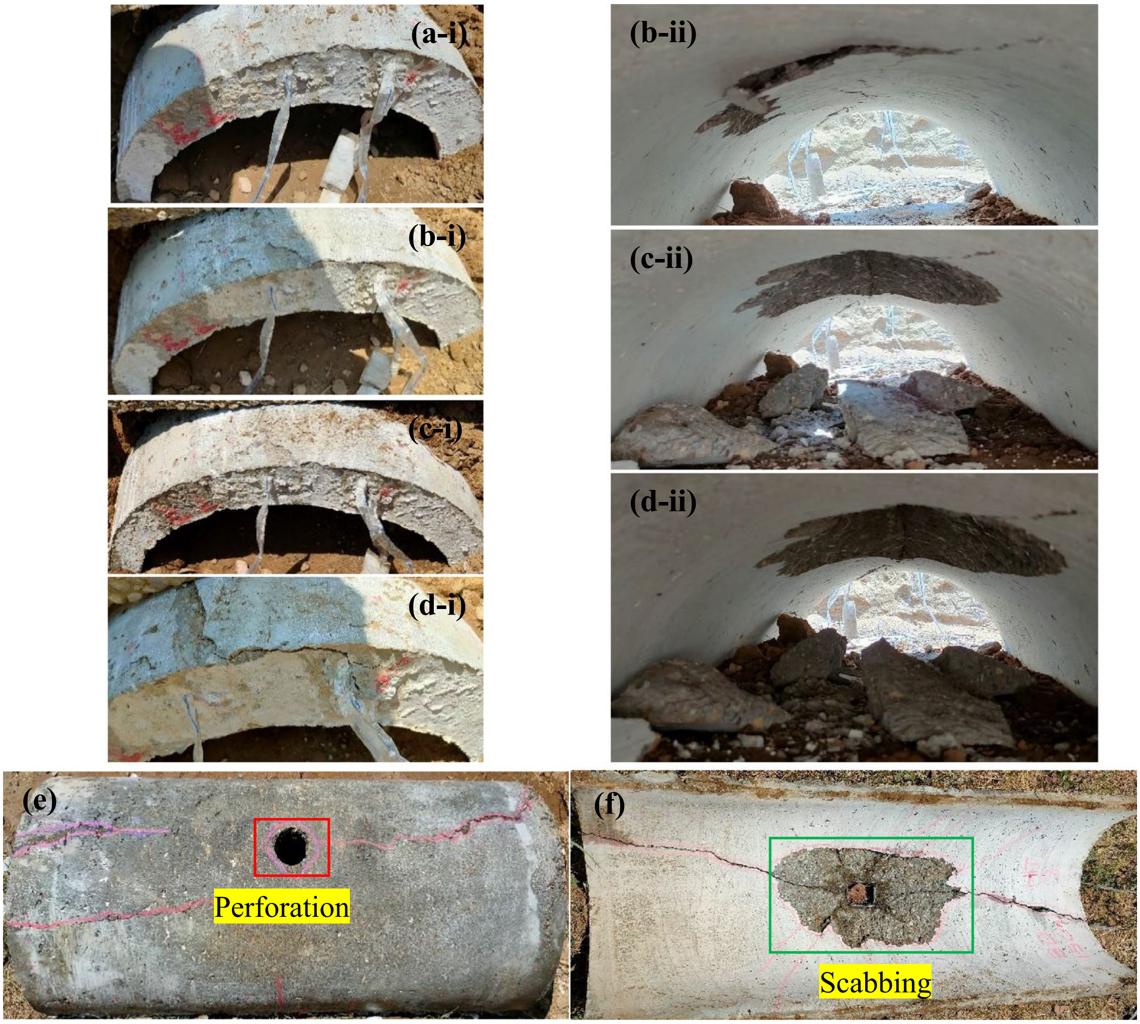

Fig. 11 Damage to the tunnel T-4-BD15 (i) side face and (ii) rear face for impact **a** 5th **b** 6th **c** 7th **d** 8th and final failure at 9th impact for **e** front and **f** rear face

depth tunnel was found to be increasing on repeated impacts, see Table 7. For 0.1 m burial depth, the peak impact force for 1st to 4th impact was 184.34, 184.21, 209.6 and 210.54 kN, respectively. It was observed that the peak impact force was increasing with each subsequent impact, see Table 7. The peak displacement for 0.1 m burial depth increased from 13.67 to 68.65 mm, indicating failure of concrete at the impacting surface. The load–displacement curve was plotted for 0.1 m burial for energy absorption calculations, see Fig. 13b. The impulse and energy absorption capacity of the tunnel was first increased from 1st to 3rd impact and then decreased for 4th impact, see Table 7.

For 0.15 m burial depth, the peak force was reduced to 155.43 kN for 1st impact. For each subsequent impact, the peak impact force was comparable to the 0.05 and 0.1 m burial depth cases, see Table 7. The load–displacement curve for 0.15 m burial depth indicates that much of the energy got absorbed into the soil layer, see Fig. 13c. Therefore, lower energy absorption values were found for the 0.15-m burial depth tunnel, see Table 7. For 0.2 m tunnel depth, there was a considerable drop in peak deformation; however, the peak force was comparable to the other cases, see Table 7. The energy absorption capacity of the tunnel was significantly lower for 0.2 m burial depth due to the lower deformations under repeated impacts, see Fig. 13d. It can be concluded that above a threshold of 0.15 m burial depth, the deformations in the tunnel can be significantly lowered. The soil cushion layer above 0.15 m was proven to be quite effective in controlling the damage to the tunnel under impact loading. For 0.25 m burial depth, the impact force was reduced as compared to earlier cases. The impact force for impact 1–4 was found to be 106, 157, 176.06 and 169.06 kN, respectively. The peak deformations in the tunnel were significantly lower than lower burial depth cases as shown in Fig. 13e. The 0.3-m burial depth observed a lower impact force for 1st impact as compared to the lower burial

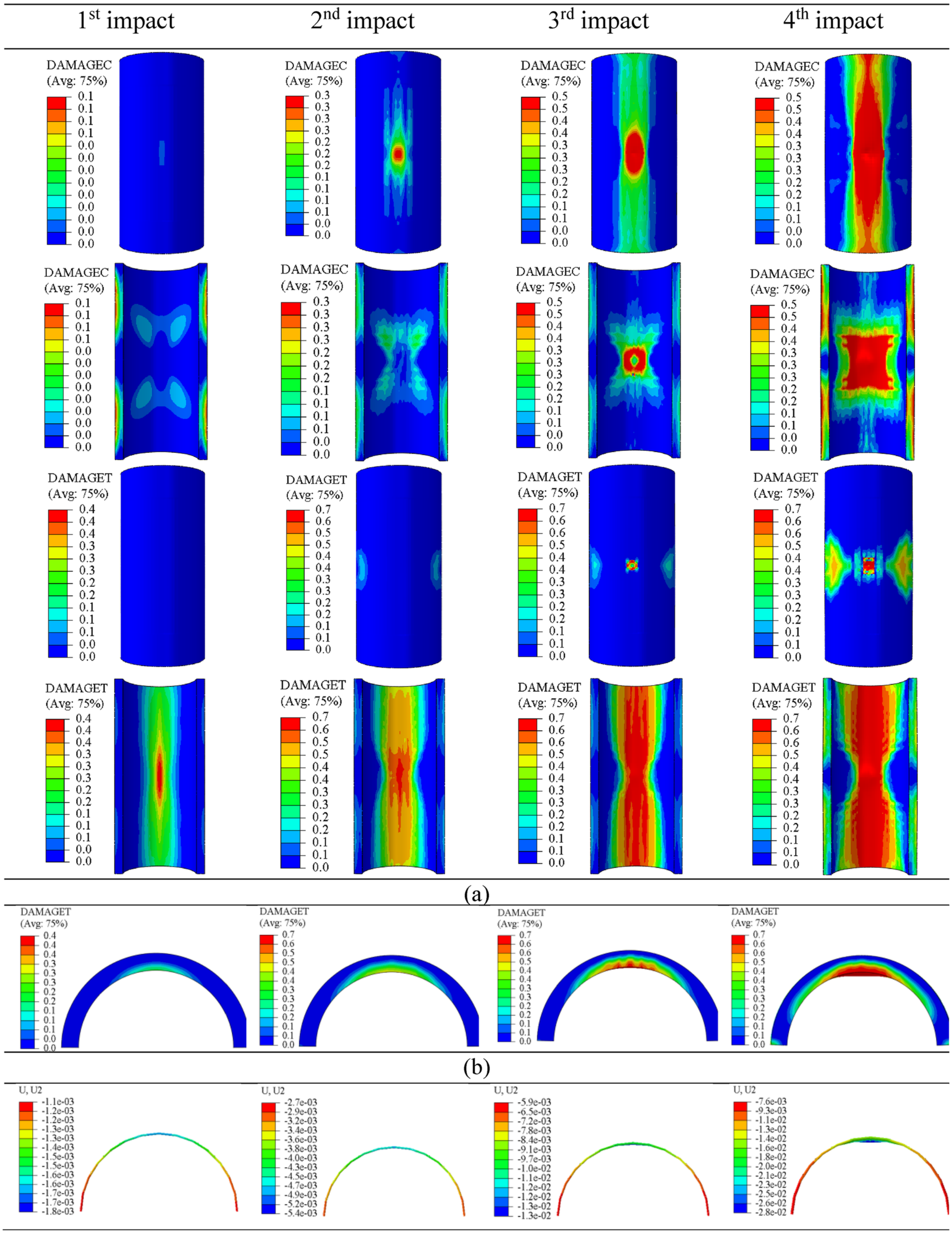

Fig. 12 Compression and tension damage to the tunnel T-4-BD15 at front and rear face under repeated impacts **a** side face and **b** displacement in rebar

depth; however, the peak force was increased for subsequent impacts and comparable to the other cases, see Table 7. The force–displacement curve was plotted for the energy absorption capacity of the tunnel as shown in Fig. 13(f). It was concluded that above 0.2 m burial depth the energy absorbed by the tunnel was similar in magnitude as well as comparable peak deformations observed. The impulse was found to be comparable for each burial depth case. Therefore, it

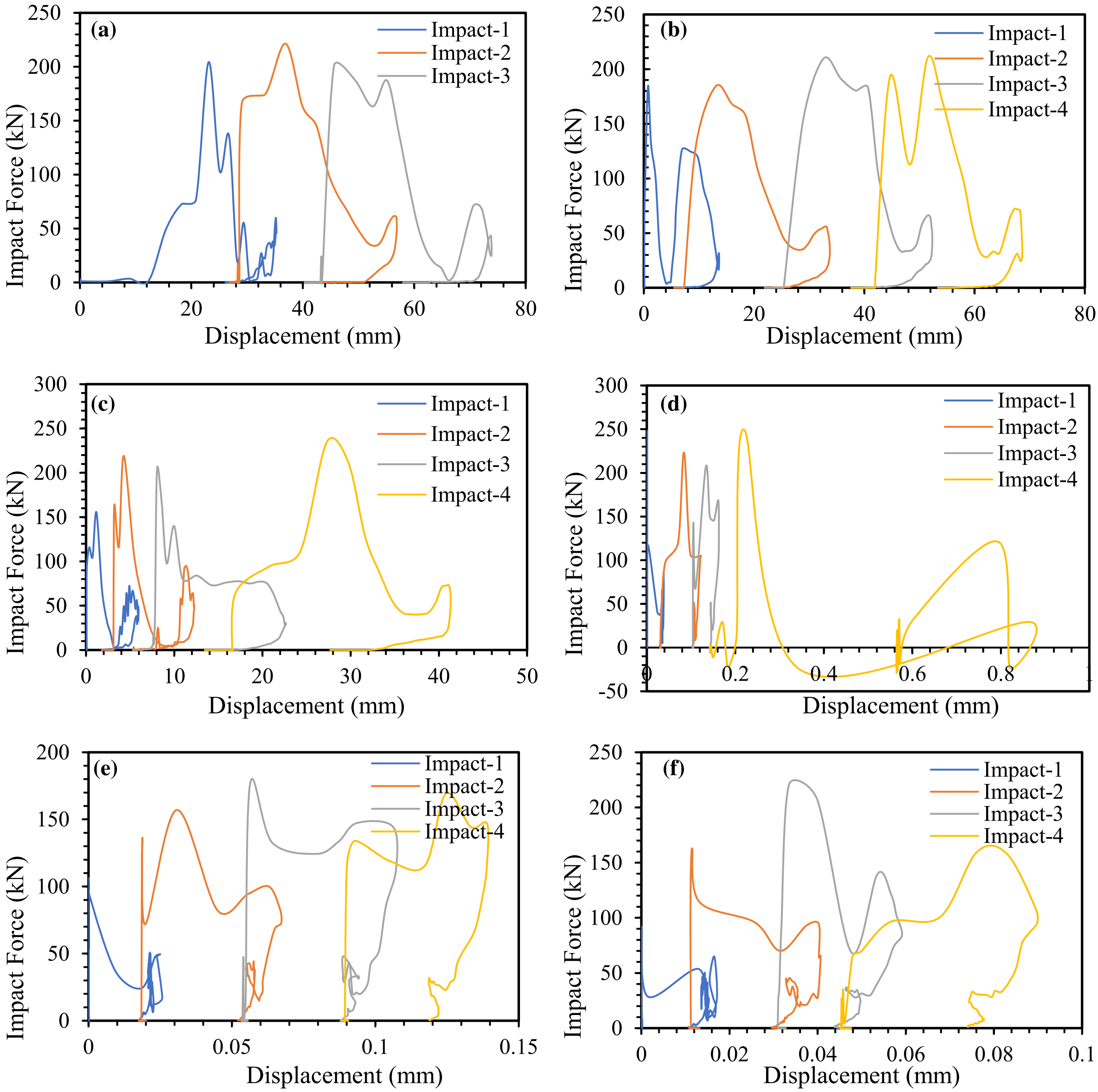

Fig. 13 Impact force–displacement curves under repeated impacts for varying burial depths of **a** 0.05 **b** 0.10 **c** 0.15 **d** 0.20 **e** 0.25 and **f** 0.30 m

was concluded that the impact duration was similar for each burial depth tunnel.

Soil Deformation Under Repeated Impact Load

The deformation of bed soil under repeated impacts was shown in Fig. 14. The deformation in the soil was increased with each subsequent impact and is presented in Table 7. For 5 mm BD the deformation in the bed soil increased to 21 mm for the 3rd impact, see Fig. 14. The deformation in bed soil was propagated longitudinally on the inner surface of the tunnel bed soil. It was observed that the deformation in the inner side of the tunnel bed soil was hogging. The soil was deformed upwards along the periphery of the tunnel due to the natural constrained boundary conditions. The deformation of the 0.10-m BD tunnel was lower for 1st impact as compared to 0.05 m

Table 7 Summary of Numerical study of tunnel under various burial depths for repeated impacts

Case	Peak force (kN)	Peak displacement in tunnel (mm)	Impulse (kN-s)	Energy absorption capacity of tunnel (kN-mm)	Peak bed soil deformation w.r.t. base position (mm)
0 m burial depth					
Impact 1	95.55	46.48	0.85	2998.62	– 18.35
Impact 2	110.38	79.34	0.91	2912.05	– 39.6
0.05 m burial depth					
Impact 1	204.32	35.27	0.93	1430.92	– 7
Impact 2	221.41	56.87	0.98	3326.07	– 15
Impact 3	200.65	73.88	0.93	3013.83	– 21
0.10 m burial depth					
Impact 1	184.34	13.67	0.90	1077.49	– 6
Impact 2	184.21	33.73	0.85	2574.60	– 13
Impact 3	209.6	52.31	0.94	3178.30	– 17
Impact 4	210.54	68.65	0.89	2810.96	– 21
0.15 m burial depth					
Impact 1	155.43	5.96	0.96	316.28	– 3.60
Impact 2	219.08	12.27	0.96	583.86	– 7.40
Impact 3	202.63	22.67	0.88	1230.62	– 12
Impact 4	234.76	41.33	0.87	2587.04	– 16
0.20 m burial depth					
Impact 1	248.36	0.04	0.89	2.55	– 0.34
Impact 2	223.26	0.12	0.81	10.27	– 0.87
Impact 3	206.48	0.16	0.93	7.53	– 1.20
Impact 4	249.56	0.86	0.17	0.58	– 1.80
0.25 m burial depth					
Impact 1	106.36	0.03	0.86	1.09	– 0.25
Impact 2	157.01	0.07	0.88	4.67	– 0.61
Impact 3	176.06	0.11	0.88	6.41	– 0.90
Impact 4	169.06	0.14	0.87	5.63	– 1.10
0.30 m burial depth					
Impact 1	91.73	0.02	0.82	0.57	– 0.24
Impact 2	162.87	0.04	0.91	2.67	– 0.52
Impact 3	220.53	0.06	1.01	3.50	– 0.66
Impact 4	159.44	0.09	0.83	4.20	– 0.83

BD; however, equal magnitude of deformation was observed below the tunnel lining for subsequent impacts, see Fig. 14. Till 0.15 m BD, the deformation in the bed soil was of equal proportions on both sides. The deformation kept on reducing as the depth of the buried soil increased. For burial depths of more than 0.15 m, the deformation primarily occurred on the left side, see Fig. 14. The hogging deformation primarily occurred on the soil directly below the tunnel. For BD 0.20 m and higher, the bed soil experiences a similar magnitude of deformation below the tunnel lining, see Fig. 14. It can be concluded that the 0.15 m soil cushion layer was most efficient and economical for the application of impact resistance for RC tunnels.

Influence of Mass and Velocity of Impactor

To study the influence of mass and impactor velocity on the behavior of underground tunnels, numerical investigations were performed on the tunnel with a constant burial depth of 0.15 m. The predicted results are presented in terms of tunnel damage, bed soil deformation and energy

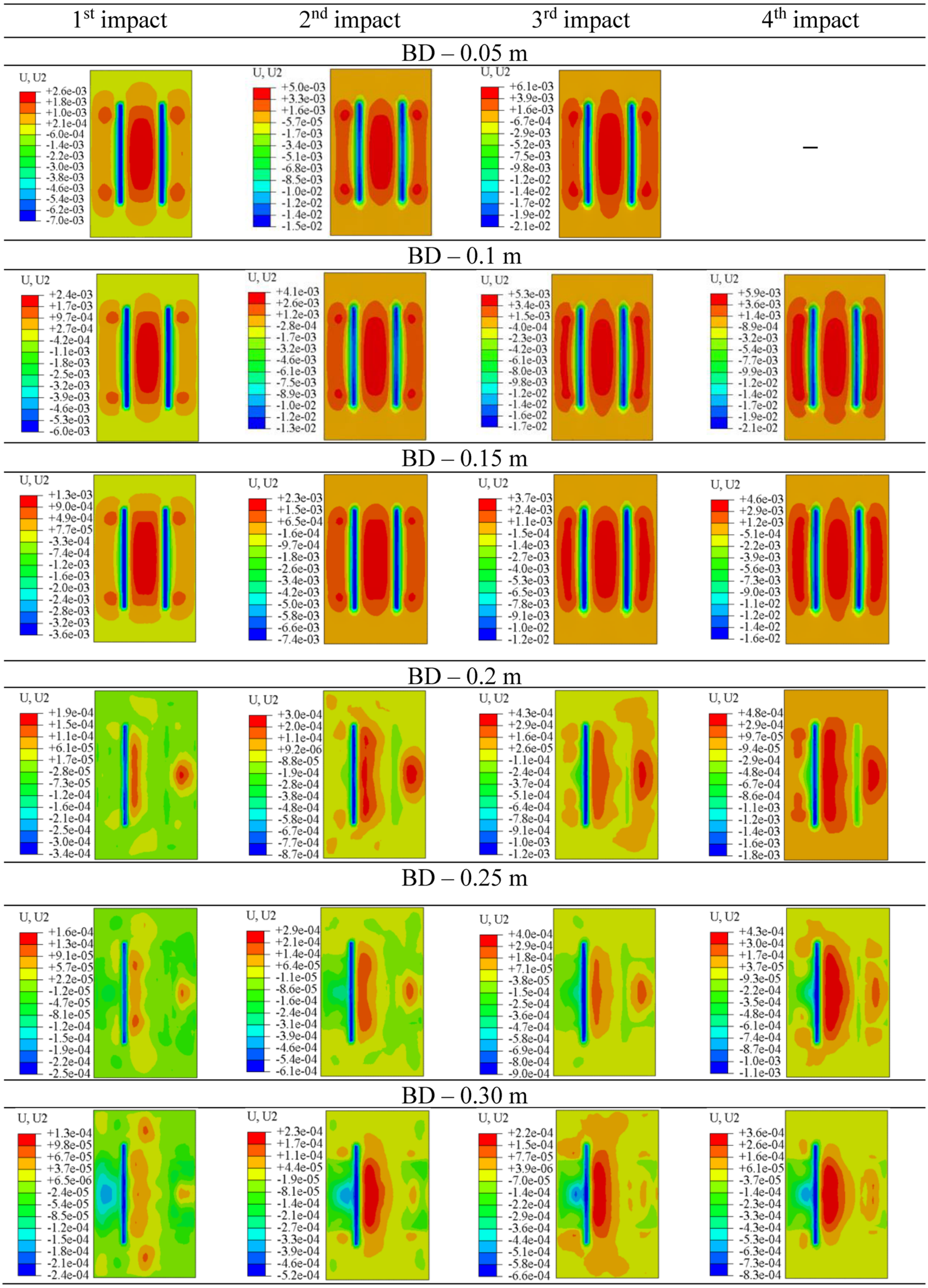

Fig. 14 Deformation in bed soil with respect to initial position for different burial depths under 1st, 2nd, 3rd, and 4th impact respectively

absorption capacity under varying the mass and velocity of the impactor.

Varying Mass of Impactor

The parametric study was performed to evaluate the damage to the tunnel for varying masses of impactor as 150, 200, 300 and 400 kg for 0.15 m soil cushion layer. The impact resistance and energy absorption capacity of the tunnel were evaluated and deformation in bed soil was also studied.

The compression and tension damage to the 0.15 m BD tunnel was evaluated of different impactor masses of 150, 200, 300 and 400 kg as shown in Fig. 15. On increasing the mass of the impactor, the compression damage to the tunnel increased longitudinally on the front face, see Fig. 15a-I, d-i. On the rear face, the compression damage was propagating radially outward from the point of impact, see Fig. 15a–ii, d–ii. As the mass of the impactor increased, the damage zone was getting enlarged for compression damage at the rear face of the tunnel. It was observed that 0.15 m BD soil was able to resist the impact till 200 kg impactor mass above which large longitudinal damage was observed. The tension damage was propagating laterally towards the free edges from the point of impact at the front face, see Fig. 15a–iii, d–iii. The damage intensity increased drastically as the mass of the impactor increases from 300 kg above, see Fig. 15c–iii, d–iii. The tension damage to the rear face of the tunnel propagated longitudinally towards the free edge, see Fig. 15a–iv, d–iv. For an impactor mass of 400 kg, the tunnel expanded radially outwards indicating complete failure along the longitudinal plane.

The impact force versus time plot of 0.15 m BD tunnel under a varying mass of impactor was shown in Fig. 16a. It was observed that the peak impact force did not show a clear trend with the change in impactor mass; however, the time history of the impact force plot for different cases was similar. The peak impact force for different cases is presented in Table 8. It was observed that the peak impact force was 308.90 kN for 400 kg mass of impactor among all other cases. It was concluded that the impact resistance of the 0.15 m BD tunnel was dependent to a lesser extent on the mass of the impactor where only slight variations in peak impact force were observed. The displacement in the tunnel for varying mass of impactor is shown in Fig. 16b. It was observed that the peak displacement was increasing with the impactor mass. It was observed that there is an abrupt change in the displacement of the tunnel after 300 kg impactor mass because the concrete elements below the impact locations were distorted and extended to larger plastic strains. The use of element erosion algorithms can ensure that the distorted elements are removed from the simulation. The peak displacement showed a linear trend with the impact mass as shown in Table 8. The peak bed soil deformation is presented in Table 8. It was observed that the peak bed soil deformation increased with the increase of impactor mass and there was an abrupt change in the deformation against 300 kg impactor mass. In addition to that, the pattern of deformation from the present study has been compared with the literature. Similar results were observed by Gahoi et al. [16] and Zaid [50] as the higher deformations due to the increase of mass of the impactor.

The impulse was calculated by integrating the impact force time history and presented in Table 8. It was observed that the impulse was increased with an increasing mass of the impactor. The impulse for the varying impactor mass was increased. The higher impulses observed were directly dependent on the higher initial impact energy to the system. The energy absorption capacity of the plate was obtained by extracting the area of the load–displacement response and the energy absorption capacity of the tunnel for varying masses of the impactor is presented in Table 8. The energy absorption capacity was increased as the mass of the impactor increased due to higher deformations observed. The increased deformations are directly related to the energy absorbed and therefore because of the absence of element removal algorithms, the plastic strains increased rapidly in the concrete.

The contours of the base soil bed deformation are presented in Fig. 17. It was observed that the negative deformations on the bed soil were mostly constricted to the base of the tunnel lining. The positive deformations occurred at the base of the tunnel where hogging moments were observed. The deformation contours were similar in nature for each case as shown in Fig. 17. The peak positive deformations for 150, 200, 300 and 400 kg were 1.9, 2.4, 4.1 and 5.8 mm as shown in Fig. 17a–d. The peak deformation showed a linear increase with increasing the mass of the impactor. The hogging deformations were mostly restricted to a smaller area around the edges of the tunnel. The area of hogging deformations increased with the increase in the mass of the impactor. The hogging deformations in bed soil below the tunnel were constricted to a smaller area as the mass of the impactor was increased, see Fig. 17a–d. The peak positive deformations were observed at the mid location below the tunnel because of the reflected compressive wave from the tunnel boundaries.

Varying Velocity of Impactor

The parametric study for varying impactor velocities of 9.9, 14, 17.15 and 19.81 ms^{-1} corresponding to the height of the impact as 5, 10, 15 and 20 m was studied for compression and tension damage. Also, the impact resistance and energy absorption capacity were studied for varying impactor velocity. Further, the deformation in the soil bed was investigated under varying impactor velocities.

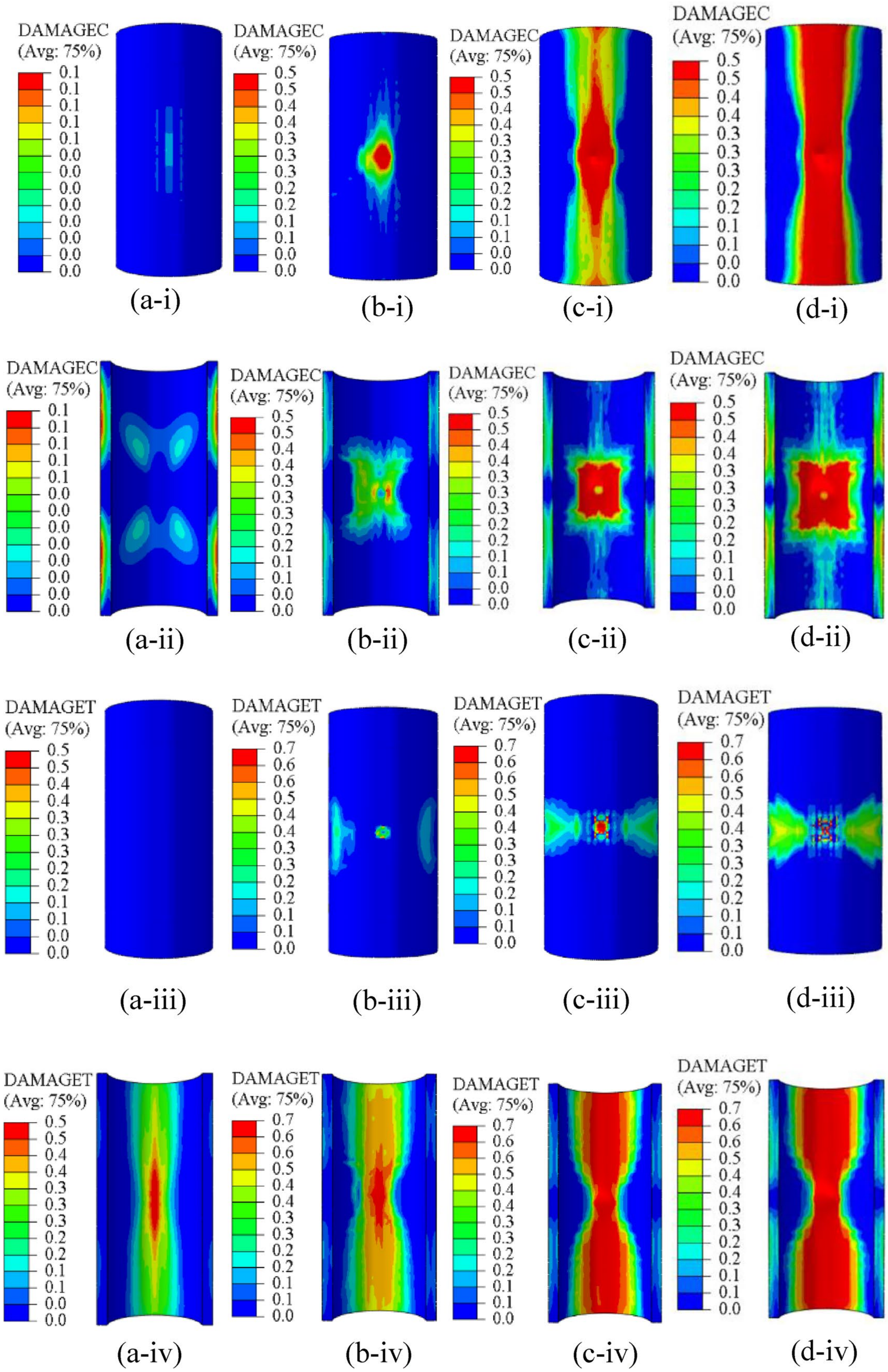

Fig. 15 (i) Front face, (ii) rear face compression damage (iii) front face and (iv) rear face tension damage for impactor mass of **a** 150 **b** 200 **c** 300 and **d** 400 kg

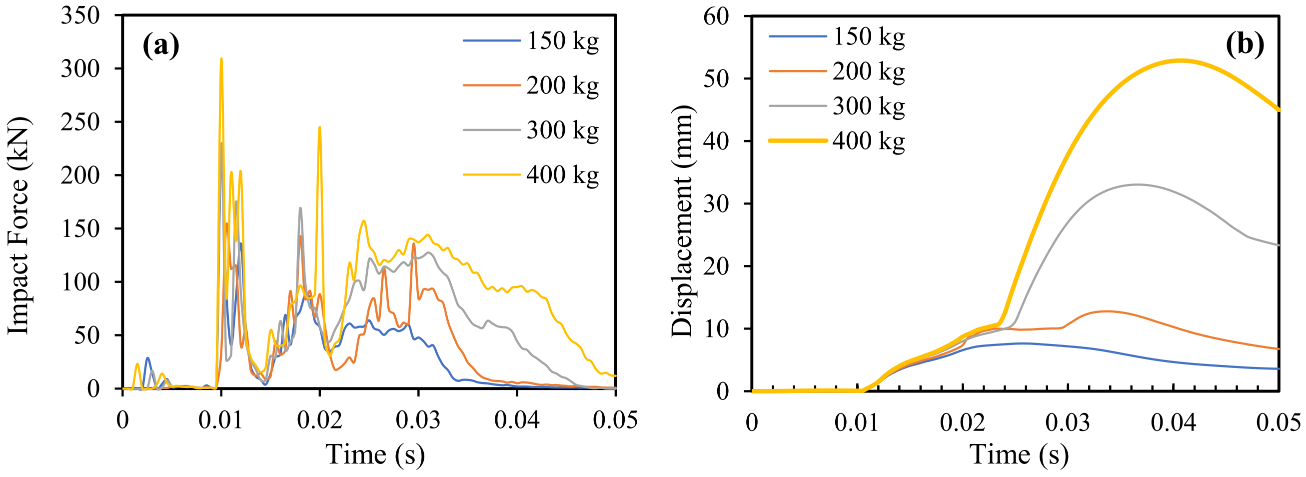

Fig. 16 **a** impact force and **b** displacement with varying mass of impactor

Table 8 Parametric analysis for varying mass of impactor

Case kg	Peak force (kN)	Peak displacement in tunnel (mm)	Impulse (kN-s)	Energy absorption capacity of tunnel (kN-mm)	Peak bed soil deformation w.r.t. base position (mm)
150	218.32	7.63	1.35	346.71	– 4.7
200	152.50	12.77	1.66	780.82	– 6.1
300	229.88	33.04	2.60	3027.69	– 11
400	308.90	52.88	3.77	5742.01	– 17

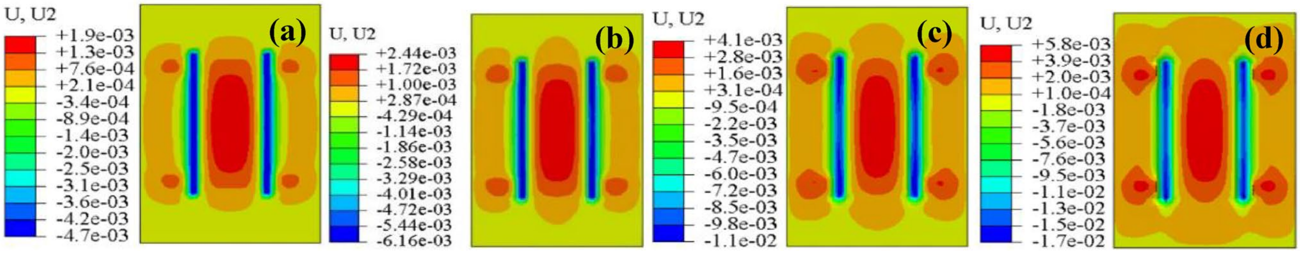

Fig. 17 Deformation (m) in soil against **a** 150 **b** 200 **c** 300 and **d** 400 kg mass impactor

The compression and tension damage to the 0.15-m BD tunnel was evaluated at different impactor velocities of 9.9, 14, 17.15 and 19.81 ms^{-1} as shown in Fig. 18. On increasing the velocity of the impactor, the compression damage to the tunnel increased longitudinally on the front face, see Fig. 18a–I, d–i. On the rear face, the compression damage was propagating radially outward from the point of impact, see Fig. Figure 18a–ii, d–ii. As the impactor velocity increased, the damage zone was getting enlarged for compression damage at the rear face of the tunnel. It was observed that 0.15 m BD soil was able to resist the impact till 14 m/s impactor mass above which large longitudinal damage was observed. The tension damage was propagating laterally towards the free edges from the point of impact at the front face, see Fig. 18a–iii, d–iii. The damage intensity was increased drastically as the impactor velocity was above 14 m/s, see Fig. 18b–iii, d–iii. As the impactor velocity increased, the tension damage at the front face started propagating in the longitudinal direction also, see Fig. 18d–iii. The tension damage to the rear face of the tunnel propagated longitudinally towards the free edge, see Fig. 18a–iv, d–iv. As the impactor velocity increased, the tension damage area along the longitudinal plane increased significantly.

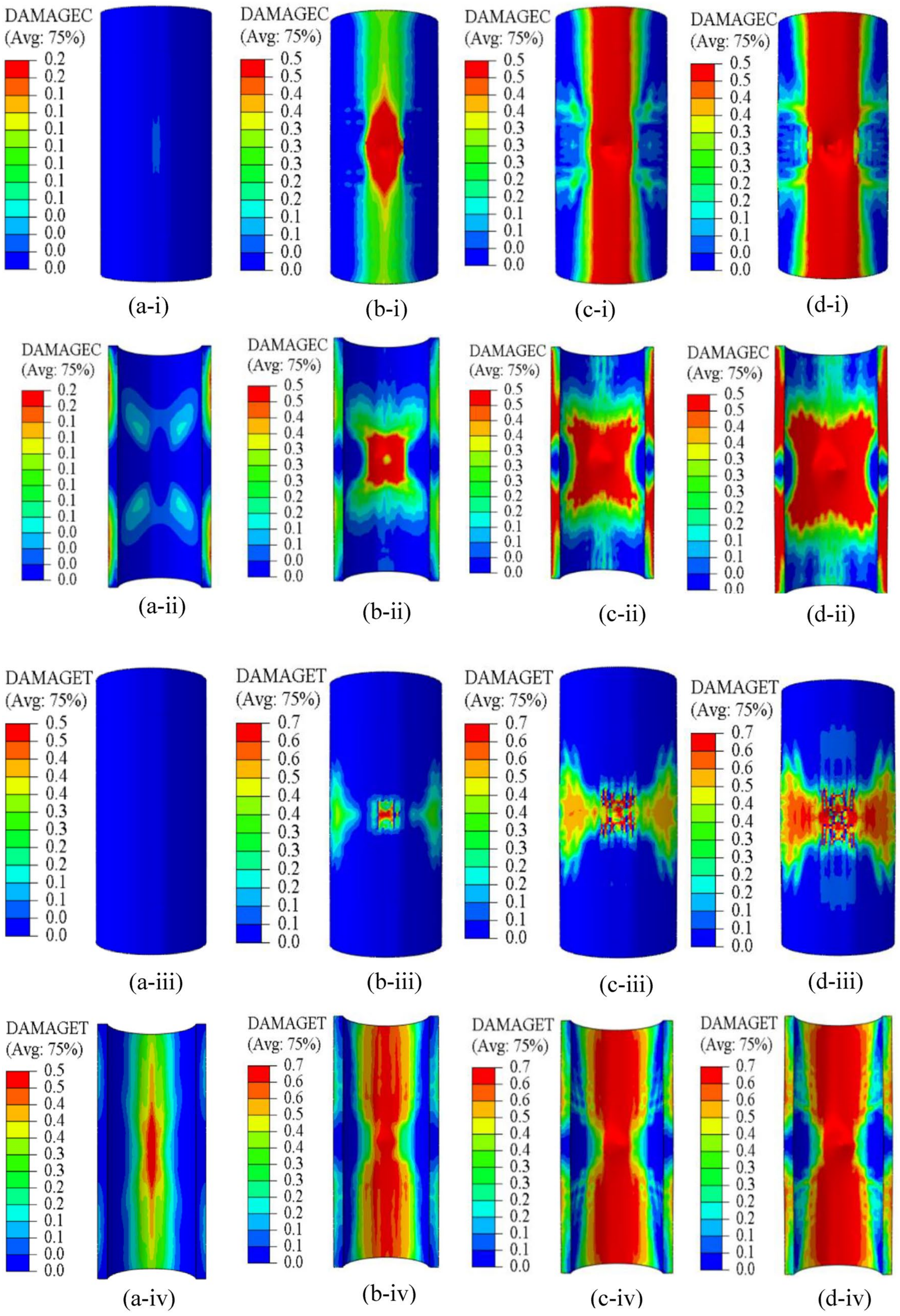

(a-i) (b-i) (c-i) (d-i)

(a-ii) (b-ii) (c-ii) (d-ii)

(a-iii) (b-iii) (c-iii) (d-iii)

(a-iv) (b-iv) (c-iv) (d-iv)

Fig. 18 (i) Front face and (ii) rear face compression damage (iii) front face and (iv) rear face tension damage under velocity of **a** 9.9 **b** 14 **c** 17.15 and **d** 19.81 ms.$^{-1}$

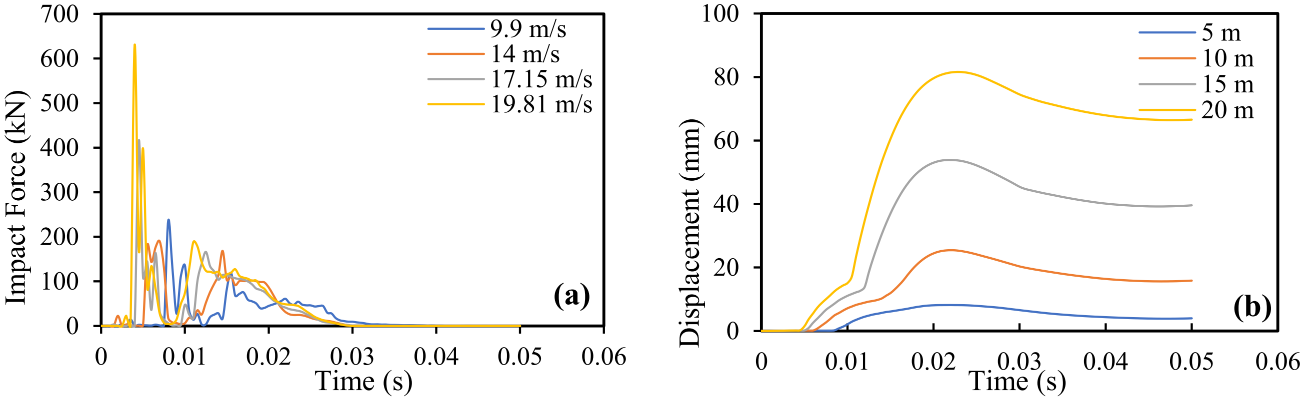

Fig. 19 Variation of **a** impact force and **b** displacement of tunnel with varying velocity of impactor

The impact force versus time plot of the 0.15 m BD tunnel under the varying velocity of the impactor was shown in Fig. 19). It was observed that a similar trend for impact force versus time plot was observed as the impactor velocity increased; however, the plateau peaks were lesser in number for 19.81 ms^{-1} impact velocity, see Fig. 19a. The peak impact force for different cases was presented in Table 9. It was observed that the peak impact force first decreased as the impactor velocity increased from 9.9–14 ms^{-1} from 235.31 to 189.33 kN and then increased significantly for 17.15 and 19.81 ms^{-1} at 416 and 630.14 kN, respectively. It was concluded that the impact resistance of the 0.15 m BD tunnel was significantly dependent on the impactor velocity. The displacement in the tunnel for varying mass of impactor is shown in Fig. 19b. The tunnel displacement versus time plot has a similar trend for change in impactor velocity, where the displacement in the tunnel first increased and then residual deformation was observed. It was observed that the peak displacement was increasing with the impactor mass, see Table 9. The peak displacements for 9.9, 14, 17.15 and 19.81 ms^{-1} were 8.17, 25.45, 53.88 and 81.59 mm, respectively. The peak bed soil deformations for different cases were presented in Table 9. It was observed that the peak bed soil deformation increased linearly with the impactor velocity.

The impulse was calculated by integrating the impact force time history and presented in Table 9. It was observed that the impulse was increased with the increasing velocity of the impactor. The impulse was increased linearly with the impactor velocity. The higher impulses observed were directly dependent on the higher initial impact energy to the system. The peak forces were much higher as the velocity of the impactor was increased; however, the impulses did not observe such behavior. Therefore, it can be concluded that the plateau of forces was similar in increasing the velocity of the impactor. The energy absorption capacity of the plate was obtained by extracting the area of the load–displacement response and the energy absorption capacity of the tunnel for the varying velocity of the impactor was presented in Table 9. The energy absorption capacity increased significantly as the velocity of the impactor increased due to higher impact forces and deformations observed. The energy absorption capacity was related to both peak force and displacement with impactor velocity and the corresponding values of energy absorption capacity for 9.9, 14, 17.15 and 19.81 ms^{-1} were 414.10, 2172.16, 5372.27 and 9922.37 kN-mm, respectively.

The contours of the base soil bed deformation were presented in Fig. 20. It was observed that the negative deformations on the bed soil were mostly constricted to the base of the tunnel lining. The positive deformations occurred at the

Table 9 Parametric analysis for varying velocity of impactor

Case ms^{-1}	Peak force (kN)	Peak displacement in tunnel (mm)	Impulse (kN-s)	Energy absorption capacity of tunnel (kN-mm)	Peak bed soil deformation w.r.t. base position (mm)
9.9	235.21	8.17	1.18	414.10	– 5.1
14	189.33	25.45	1.50	2172.16	– 12
17.15	416.32	53.88	1.70	5372.27	– 17
19.81	630.14	81.59	2.30	9922.37	– 20

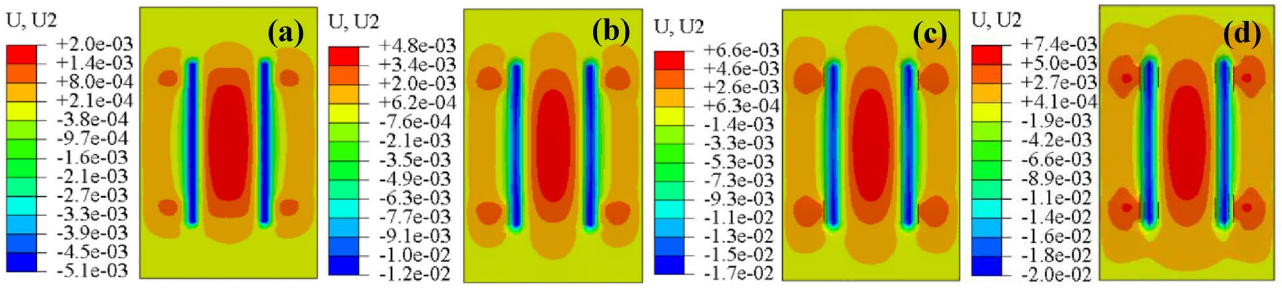

Fig. 20 Deformation in soil bed for impactor velocity **a** 9.9 **b** 14 **c** 17.15 and **d** 19.81 ms.$^{-1}$

base of the tunnel where hogging moments were observed. The deformation contours were similar in nature for each case as shown in Fig. 20. The peak positive deformation for 9.9, 14, 17.15 and 19.81 ms^{-1} were 2, 4.8, 6.6 and 7.4 mm as shown in Fig. 20a—d. The peak deformation showed a linear increase with increasing the impactor velocity from 2.0 to 7.4 mm. The hogging deformations were mostly restricted to a smaller area around the edges of the tunnel. The area of hogging deformations increased with the increase in the velocity of the impactor, see Fig. 20d. The hogging deformations in bed soil below the tunnel were constricted to a smaller area as the velocity of the impactor was increased, see Fig. 20a–d. The peak positive deformations were observed at the mid location below the tunnel because of the reflected compressive wave from the tunnel boundaries and as the impactor velocity increased the waves got constricted at the middle.

Analytical Evaluation

The numerical results were compared with the analytical methods available in the literature for the prediction in peak impact force with varying soil cushion depth, see Fig. 21a. The Swiss, Japanese and Australian algorithms did not have considerations for soil cushion layer depth, whereas the Chinese tunnel manual algorithm consider the effect of soil cushion. It was observed that the Chinese tunnel manual algorithm predicts the peak impact force much less as compared to numerical results. However, all other algorithms have good predictions for peak impact force for 0 m burial depth and 0.25 and 0.3 m burial depths. The use of numerical simulations is further compared with analytical methods for varying impactor mass and velocity, see Fig. 21b and c. It was observed that the analytical methods underpredict the peak impact force as compared to numerical methods. However, on increasing the mass of the impactor, the prediction accuracy improved, and optimum prediction accuracy was observed for Yang Qixin's algorithm. The Australian algorithm overpredicts the peak impact force with higher impactor velocity. For better prediction, R_c parameter which

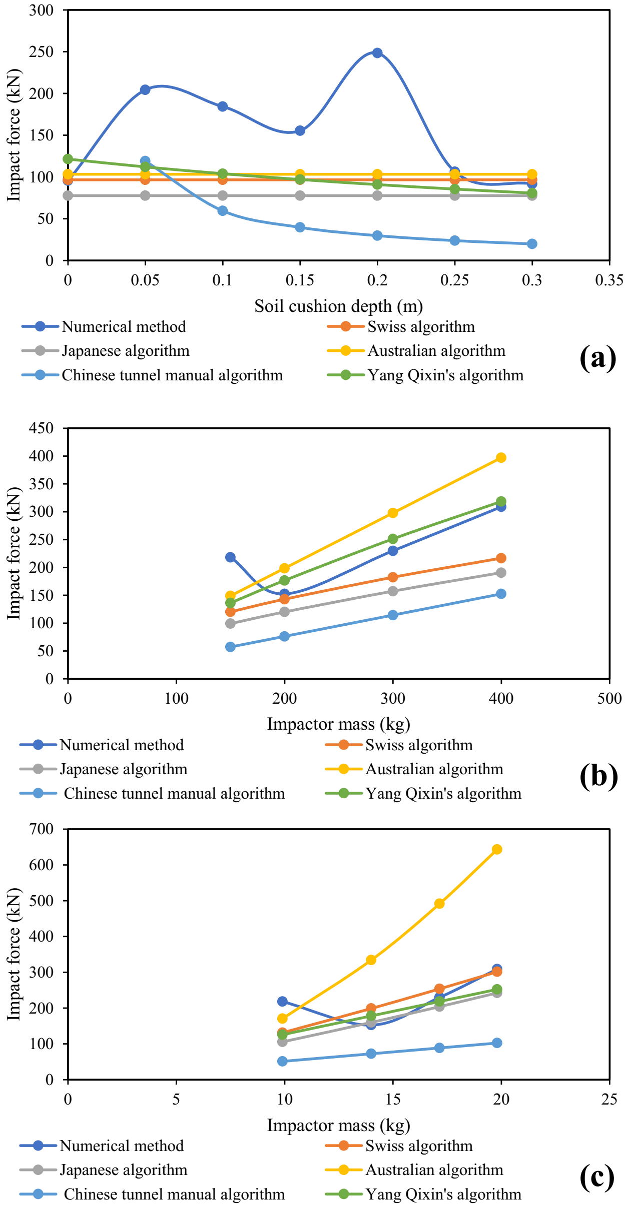

Fig. 21 Comparison of analytical methods with numerical simulation for varying **a** soil cushion depth **b** impactor mass and **c** impactor velocity

is described as the indentation resistance needs to be calibrated. In the present study, numerical results on varying velocities of the impactor, match well with the analytical algorithms. Similar to impactor velocity, the Australian algorithm overestimates the peak impact force as compared to other methods for higher mass. However, the numerical methods showed similar results compared with the other methods and can be used as a benchmark for the design and evaluation of concrete tunnels under impact loading.

Conclusions

The experimental and numerical investigation on reinforced concrete tunnels was performed for varying burial depths of soil cushion layer under low-velocity impact. The tunnels were investigated experimentally considering 0.05, 0.1 and 0.15 m of soil cushion layer. The numerical study was performed for tunnels under repeated impacts for evaluation of the peak force, displacement, and energy absorption capacity of the tunnel. The parametric study was performed for the impact resistance and energy absorption of the tunnel for varying mass and velocity of the impactor. Based on the study, the following conclusions were drawn:

- The resistance of the tunnel was found to be increasing significantly as the burial depth of soil was increased from 0.05 to 0.1 m. The mode of failure was changing with each subsequent impact for the 0 and 0.05 m BD tunnel; however; for 0.1 and 0.15 m the mode of failure was the same till the 5th and 6th impact and after that, the mode of failure was changed to punching shear failure.
- It was concluded that the numerical results were in good agreement with the experimental results for peak displacement and strain in rebar. The peak displacement was reduced by increasing the burial depth of the soil and negligible displacement was observed for a burial depth of 0.20 m or higher.
- The impulses were found to be independent of soil burial depth. Further, the energy absorption capacity of the tunnel was found to be increasing with each subsequent impact for 0, 0.05, 0.1 and 0.15 m tunnel burial depth. For 0.2 m and higher BD, very less energy absorption was observed in the tunnel because the burial soil absorbed most of the impact energy.
- It was observed that the impact force did not have a clear trend for change in the mass of the impactor. The impulse was increasing with the mass of the impactor indicating higher plateau forces for a larger mass of the impactor. Further, the energy absorption capacity was increasing as the mass of impactors increased.
- The peak force first decreased and then increased significantly as the velocity of the impactor increased, however, the impulses were increasing with increasing velocity highlighting that the plateau of impact force was increasing. The energy absorption capacity of the tunnel also increased significantly as the velocity of the impactor increases due to the higher force and displacement observed for higher velocities.
- The bed soil deformations were increasing with both impactor mass as well as impactor velocity. The hogging deformations were observed below the tunnel and were restricted to the mid location on increasing mass and velocity of the impactor.
- The numerical simulations agreed with the analytical methods for peak impact under varying mass and velocity of the impactor. It was observed that Yang Qixin's algorithm was best among other predicting algorithms when comparing peak impact force with the numerical result.

Acknowledgements This work is part of the research project "Safeguarding civil underground tunnels against terrorist blast and explosion shocks". This is a "Royal Society Yusuf Hamied International Exchange Award" funded by The Yusuf and Farida Hamied Foundation, with contract number IES\R2\181054. Their contribution is gratefully acknowledged.

Data availability Data used to support the findings of this study will be made available on request basis.

References

1. Vittorio G, Piergiorgio G, Ashraf M, Shulin X (2008) Mechanized tunnelling in urban areas: design methodology and construction control. CRC Press
2. Degn Eskesen S, Tengborg P, Kampmann J, Holst VT (2004) Guidelines for tunnelling risk management: international tunnelling association, working group No 2. Tunn Undergr Sp Technol 19:217–237
3. Kusakabe O, Takemura J, Takahashi A, Izawa J, Shibayama S (2008) Physical modeling of seismic responses of underground structures. Int. Conf. Int Assoc Comput Methods Adv Geomech 6:1459–1474
4. He W, Wu Z, Kojima Y, Asakura T (2009) Failure mechanism of deformed concrete tunnels subject to diagonally concentrated loads. Comput Civ Infrastruct Eng 24:416–431
5. Asakura T, Kojima Y (2003) Tunnel maintenance in Japan. Tunn Undergr Sp Technol 18:161–169
6. Li Y, Jin X, Lv Z, Dong J, Guo J (2016) Deformation and mechanical characteristics of tunnel lining in tunnel intersection between subway station tunnel and construction tunnel. Tunn Undergr Sp Technol 56:22–33
7. Wang Z, Xie Y, Liu H, Feng Z (2021) Analysis on deformation and structural safety of a novel concrete-filled steel tube support system in loess tunnel. Eur J Environ Civ Eng 25:39–59
8. Mishra S, Rao KS, Gupta NK, Kumar A (2017) Damage to shallow tunnels under static and dynamic loading. Procedia Eng 173:1322–1329

9. Mishra S, Kumar A, Rao KS, Gupta NK (2021) Experimental and numerical investigation of the dynamic response of tunnel in soft rocks. Structures 29:2162–2173
10. Liu W, Chen J, Chen L, Luo Y, Shi Z, Wu Y, Chen J, Chen L (2020) Nonlinear deformation behaviors and a new approach for the classification and prediction of large deformation in tunnel construction stage : a case study. Eur J Environ Civ Eng 26:1–29
11. Wang WL, Wang TT, Su JJ, Lin CH, Seng CR, Huang TH (2001) Assessment of damage in mountain tunnels due to the Taiwan Chi-Chi Earthquake. Tunn Undergr Sp Technol 16:133–150
12. Zhao P, Xie L, Li L, Liu Q, Yuan S (2018) Large-scale rockfall impact experiments on a RC rock-shed with a newly proposed cushion layer composed of sand and EPE. Eng Struct 175:386–398
13. Hu J, Li S, Li L, Shi S, Zhou Z, Liu H (2018) Field, experimental, and numerical investigation of a rockfall above a tunnel portal in southwestern China. Bull Eng Geol Environ 77:1365–1382
14. Hu J, Li S, Shi S, Zhang J, Xian G (2019) Development and application of a model test system for rockfall disaster study on tunnel heading slope. Environ Earth Sci 78:391
15. Dhamne RR, Mishra S, Kumar A, Rao KS (2021) Deformation behavior of D-Shaped shallow tunnels under dynamic loading conditions. Structures 33:3973–3983
16. Gahoi A, Zaid M, Mishra S, Rao KS (2017) Numerical analysis of the tunnels subjected to impact loading. 7th Indian rock Conf. (IndoRock2017). Indorock2017, New Delhi
17. Mishra S, Zaid M, Rao KS, Gupta NK (2021) FEA of urban rock tunnels under impact loading at targeted velocity. Geotech Geol Eng 40:1693–1711
18. Rao KS, Sarmah R, Mishra S (2015) Effect of projectile penetration on shallow tunnels. 50th Indian Geotech. Conf. 17th-19th December 2015, Pune, Maharashtra
19. Meng G, Gao B, Zhou J, Cao G, Zhang Q (2016) Experimental investigation of the mechanical behavior of the steel fiber reinforced concrete tunnel segment. Constr Build Mater 126:98–107
20. Yan Q, Li B, Geng P, Chen C, He C, Yang W (2016) Dynamic response of a double-lined shield tunnel to train impact loads. Tunn Undergr Sp Technol 53:33–45
21. Sharma H, Mishra S, Rao KS, Gupta NK. Effect of cover depth on deformation in tunnel lining when subjected to impact load. ISRM Int. Symp. Asian Rock Mech. Symp., OnePetro: 2018, p. 978–981
22. Wang S, Liu Y, Du K, Zhou J (2019) Dynamic failure properties of sandstone under radial gradient stress and cyclical impact loading. Front Earth Sci. https://doi.org/10.3389/feart.2019.00251
23. Wang H, Guo C, Wang F, Ni P, Sun W (2022) Peridynamics simulation of structural damage characteristics in rock sheds under rockfall impact. Comput Geotech 143:104625
24. Woods RD (1968) Screening of surface wave in soils. J Soil Mech Found Div 94:951–979
25. Bhatti AQ, Kishi N, Shad KUR (2008) A numerical investigaton for rock fall impact behaviour of pit head of tunnel with falling weight impact loading. In: 10th International Ls-Dyna user conference. Dearborn, Michigan
26. Volkwein A, Schellenberg K, Labiouse V, Agliardi F, Berger F, Bourrier F, Dorren LKA, Gerber W, Jaboyedoff M (2011) Rockfall characterisation and structural protection – a review. Nat Hazards Earth Syst Sci 11:2617–2651
27. Rezagholilou A, Nikraz H (2013) Protective layer for tunnels under rock fall impacts. Proc World Tunn Congr WTC 2013:1632
28. Baziar MH, Shahnazari H, Kazemi M (2018) Mitigation of surface impact loading effects on the underground structures with geofoam barrier: Centrifuge modeling. Tunn Undergr Sp Technol 80:128–142
29. Zaid M (2021) Dynamic stability analysis of rock tunnels subjected to impact loading with varying UCS. Geomech Eng 24:505–518
30. Xu ZH, Wang WY, Lin P, Wang XT, Yu TF (2020) Buffering effect of overlying sand layer technology for dealing with rockfall disaster in tunnels and a case study. Int J Geomech 20:04020127
31. Pichler B, Hellmich C, Mang HA (2005) Impact of rocks onto gravel Design and evaluation of experiments. Int J Impact Eng 31:559–578
32. Dhamne R, Mishra S, Kumar A, Rao KS (2018) Numerical study of the cross-sectional shape of shallow tunnels subjected to impact and blast loading. Natl Conf Prospect Retrosp Eng Geol Geophys Instrum 43:23–37
33. Li Y, Zhang S, Xu J (2011) Experimental research on dynamic model material of high concrete dam. Rock Soil Mech 32:757–761
34. Liu X, Sheng Q, Chen J, KE W, Yang J. (2015) Seismic shaking table test for large-scale underground cavern group (II): test scheme. Rock Soil Mech 36:1683–1690
35. Kutter BL (1992) Dynamic centrifuge modeling of geotechnical structures. Transp Res Rec p. 24–30
36. Verma AK, Sardana S, Sharma P, Dinpuia L, Singh TN (2019) Investigation of rockfall-prone road cut slope near Lengpui Airport, Mizoram. India J Rock Mech Geotech Eng 11:146–158
37. Stoffel FDSM (1998) Order To Assess the Technical Possibilities of Individual Rockfalls p. 37–47
38. IS: 10262. Concrete mix proportioning—guidelines. Bur Indian Stand New Delhi 2019
39. IS 456: Code of practice for plain and reinforced concrete. Bureau of Indian Standards, New Delhi, India; 2000
40. China PR, of. (2017) Test methods of concrete and reinforced concrete sewer pipes. People's Republic of China, Beijing
41. Ni P, Shen L, Mei G, Jiang P (2022) Load capacity of perforated reinforced concrete sewer pipes. J Pipeline Syst Eng Pract 13:04021065
42. Hrynyk TD, Vecchio FJ (2017) Modeling of reinforced and fiber-reinforced concrete slabs under impact loads. Am Concr Institute, ACI Spec Publ p. 118–37
43. Labiouse V, Descoeudres F, Montani S (1996) Experimental study of rock sheds impacted by rock blocks. Struct Eng Int 6:171–176
44. Kishi N, Ikeda K, Konno H, Kawase R (2000) Prototype impact test on rockfall retaining walls and its numerical simulation. WIT Trans Built Environ 48
45. Qixin Y, Baoshu G (1996) Test and research on calculating method of falling stone impulsive force. J China Railw Soc 18:101–106
46. Luo FJ, Zhou XJ, Wang Y, Zhang FL (2018) Experimental study on rockfall impact force applied to frame shed tunnels. J Highw Transp Res Dev 12:59–66
47. Lubliner J, Oliver J, Oller S, Oñate E (1989) A plastic-damage model for concrete. Int J Solids Struct 25:299–326
48. Lee J, Fenves GL (1998) Plastic-damage model for cyclic loading of concrete structures. J Eng Mech 124:892–900
49. Gupta I (2019) Experimental and Numerical Studies on the Resilience capacity of the Reinforced Concrete Tunnel Against Free-Fall Impact Loading. Dissertation of Master of Technology, Submitted to Dr B R Ambedkar NIT Jalandhar, Punjab
50. Zaid M (2021) Preliminary Study to Understand the Effect of Impact Loading and Rock Weathering in Tunnel Constructed in Quartzite. Geotech Geol Eng
51. Hafezolghorani M, Hejazi F, Vaghei R, Bin JMS, Karimzade K (2017) Simplified damage plasticity model for concrete. Struct Eng Int 27:68–78
52. Johnson GR, Cook WH (1985) Fracture characteristics of three metals subjected to various strains, strain rates, temperatures and pressures. Eng Fract Mech 21:31–48

53. Iqbal MA, Rai S, Sadique MR, Bhargava P (2012) Numerical simulation of aircraft crash on nuclear containment structure. Nucl Eng Des 243:321–335
54. Kumar V, Kartik KV, Iqbal MA (2020) Experimental and numerical investigation of reinforced concrete slabs under blast loading. Eng Struct 206:110125
55. DS Simulia Corp (2019) ABAQUS/CAE User's Guide, Dassault Systèmes (DS) Simulia Corp. RI, USA
56. Kim D-J, Youn J-U, Jee S-H, Choi J, Lee J-S, Kim D-S (2014) Numerical studies on bearing capacity factor N γ and shape factor of strip and circular footings on sand according to dilatancy angle. J Korean Geotech Soc 30:49–63
57. Meyerhof GG (1963) Some recent research on the bearing capacity of foundations. Can Geotech J 1:16–26
58. Maranha JR (2009) The experimental determination of the angle of dilatancy in soils. Geotech Eng p. 147–50.
59. Zhou J, Wen P, Wang S (2020) Numerical investigation on the repeated low-velocity impact behavior of composite laminates. Compos Part B Eng 185:107771